The Thesis Committee for Hyungjoo Lee
Certifies that this is the approved version of the following thesis:

Invasion-Consistent Interpretation of Multi-Dimensional Magnetic Resonance Measurements

APPROVED BY
SUPERVISING COMMITTEE:

Supervisor:

Carlos Torres-Verdín

Hugh Daigle

Invasion-Consistent Interpretation of Multi-Dimensional Magnetic Resonance Measurements

by

Hyung Joo Lee, B.S.E

Thesis

Presented to the Faculty of the Graduate School of

The University of Texas at Austin

in Partial Fulfillment

of the Requirements

for the Degree of

Master of Science in Engineering

The University of Texas at Austin

December 2013

Dedication

This thesis is dedicated to my loving family.

Acknowledgements

First and foremost, I am deeply grateful to Dr. Carlos Torres-Verdín, for his encouragement, guidance, and support during this research. His supervision and inspiration led me to learn new ideas and gain valuable experiences. I am also pleased to thank Dr. Hugh Daigle, for his valuable comments as the second reader of this thesis.

I particularly would like to acknowledge German Merletti, of BP, for providing the well logs and corresponding NMR measurements used in this study. His technical comments helped me to analyze the well data.

I express my gratitude to members of the formation evaluation group at The University of Texas at Austin. Credit is given to Rey Casanova for his administrative assistance. I am grateful to Ben Voss and Paul Linden for UTAPWeLS software support. Many thanks go to Dr. Emmanuel Toumelin and Kanay Jerath for their advice and help in understanding NMR physics. I wish to thank all my colleagues in our group for making insightful suggestions and for our constructive discussions.

Frankie Hart and Dr. Roger Terzian are also recognized for contributing their administrative and technical support. Special thanks go to my family and friends in Korea and my new friends here in Texas for their never-ending support and love.

The work reported in this thesis was funded by The University of Texas at Austin's Research Consortium on Formation Evaluation, jointly sponsored by Afren, Anadarko, Apache, Aramco, Baker-Hughes, BG, BHP Billiton, BP, Chevron, China Oilfield Services, Ltd., ConocoPhillips, ENI, ExxonMobil, Halliburton, Hess, Maersk, Marathon Oil Corporation, Mexican Institute for Petroleum, Nexen, ONGC, Petrobras,

Repsol, RWE, Schlumberger, Shell, Statoil, Total, Weatherford, Wintershall, and Woodside Petroleum Limited.

Abstract

Invasion-Consistent Interpretation of Multi-Dimensional Magnetic Resonance Measurements

Hyung Joo Lee, M.S.E

The University of Texas at Austin, 2013

Supervisor: Carlos Torres-Verdín

This thesis introduces a workflow to accomplish invasion-consistent Nuclear Magnetic Resonance (NMR) measurement interpretations. Magnetic resonance measurements are affected by mud-filtrate invasion because the radial depth of investigation (DOI) of NMR logging tools is very shallow (approximately 1 to 4 inches). This characteristic indicates that identification of in-situ fluid saturations from NMR measurements is uncertain. Calculation of fluid saturations from apparent electrical resistivities and nuclear logs does not guarantee a precise estimation of the fluid distributions. Free water in the reservoir displaced by oil based mud (OBM) poses more challenges in the estimation of in-situ fluid saturations. To mitigate this ambiguity, I construct layer-by-layer static and dynamic reservoir models.

The common stratigraphic framework (CSF) proposed by Voss et al. (2009) was used to construct the earth model. Appraisal of static petrophysical properties is based on the iterative adjustments to minimize the discrepancy between available well logs and their numerical simulations. Evaluation of dynamic petrophysical properties can be achieved with the simulation of mud-filtrate invasion. This simulation can assess accurate fluid saturations at specific radial distances. In addition, numerically simulated apparent resistivity and nuclear logs are in agreement with measured logs.

Algorithms are also developed to cross-validate NMR measurements based on the assumption of spherically shaped water-wet pores. The algorithms need all petrophysical parameters and fluid saturations yielded from the dynamic model as inputs. Various NMR parameter changes were tested to validate this algorithm. Examples of NMR responses include wettability change and kerogen contained in nano-scale pores. For the field case examples, two 15 meter-thick depth intervals in oil- and gas-bearing siliciclastic formations were selected. Two-dimensional (2D) NMR simulations were performed with petrophysical parameters provided from the numerical simulation of mud-filtrate invasion. The 2D NMR maps are more favorable in fluid typing than conventional NMR T_2 distributions because they contrast fluid diffusion coefficient. Comparisons of simulation results to inversion results confirm the validity of the workflow introduced in this thesis for the quantification of virgin reservoir fluids and mud-filtrate saturations.

Finally, forward modeling and inversion processes are applied to 2D NMR data. The reconstructed echo decay sequences are more advantageous than raw measurements

because of their higher signal to noise ratio (SNR). Linear inversion using these echo decay sequences provides proton density distribution functions of D-T_2 and T_1-T_2 maps. Application of inversion to the two field cases measured from two different radial depths verifies the validity of the NMR interpretations.

Table of Contents

List of Tables

List of Figures

Chapter 1: Introduction

This thesis discusses the interpretation of nuclear magnetic resonance (NMR) measurements acquired in reservoir rocks. Most NMR logging tools have very shallow sensing characteristics, responses can be affected by mud-filtrate invasion. Consequently, numerical simulation of the mud-filtrate invasion process helps one to produce invasion-consistent interpretations of NMR measurements.

1.1 INTRODUCTION

NMR logging has increasingly been applied in petrophysical formation evaluation. The primary applications of NMR logs are to quantify the total porosity of reservoir rocks, to predict pore size distributions, and to distinguish and quantify types of fluids present in the rock. NMR logging also provides an indirect estimation of permeability by using a relationship between irreducible water saturation and movable fluid saturations (Timur, 1969; Kenyon et al., 1989; Straley et al., 1994). The advantage of the NMR technique over other logging methods is sensitivity to pore fluids because it measures only magnetization of mobile hydrogen nuclei. Whereas porosity estimations using neutron, density, and sonic logs require matrix properties, NMR porosity is independent of lithology. Therefore, it is unnecessary to calibrate to specific lithology (Coates et al., 1999). Also, NMR logging tools can make multiple frequencies to regulate different depth of investigations (DOIs).

Modern NMR logging tools measure several echo decay sequences in two steps. The first step is to build-up magnetizations of hydrogen nuclei. In a reservoir, net magnetization is originally zero because hydrogen nuclei are randomly oriented. When the NMR logging tool passes through the formation, the magnets create a static field

vector, B_0, to polarize hydrogen nuclei in the longitudinal direction. During the polarization time, *TW*, net magnetization increases exponentially until reaching the asymptote value, M_0. The longitudinal relaxation time, T_1, represents how fast a fluid can become polarized in a magnetic field.

The second step is to apply a pulsed oscillating magnetic field, B_1. After hydrogen nuclei become fully polarized, B_1 is applied perpendicular to B_0 to tip the magnetization to a transverse direction. The application of B_1 to hydrogen nuclei causes phase precession, which is known as nuclear magnetic resonance. Radio frequency (RF) pulses can be expressed in angular-pulse terms such as 90° pulse and 180° pulse, thus describing the magnetization angle tipped by B_1. The RF pulse train has one 90° pulse followed by a set of 180° pulses. The spin echoes are measured between these 180° pulses, which are evenly spaced with inter-echo time, *TE*. These spin echoes and the RF pulse trains are known as the Carr-Purcell-Meiboom-Gill (CPMG) sequence (Carr and Purcell, 1954; Meiboom and Gill, 1958). The CPMG is the most popular sequence in NMR logging. The amplitude of spin echo decays exponentially with the transverse relaxation time. This constant time, known as T_2, represents how fast a fluid can lose its magnetizations; T_1 and T_2 can be calculated by mathematical inversions using echo decay sequences, which will be discussed in Chapter 6. Traditional interpretation of NMR measurements uses both longitudinal relaxation time and transverse relaxation time distributions, as shown in **Figure 1.1**. The equations governing T_1 and T_2 can be expressed as

$$\frac{1}{T_1} = \frac{1}{T_{1bulk}} + \rho_1 \frac{S}{V}, \tag{1.1}$$

and

$$\frac{1}{T_2} = \frac{1}{T_{2bulk}} + \rho_2 \frac{S}{V} + \frac{D(\gamma GTE)^2}{12}, \tag{1.2}$$

where ρ_1 and ρ_2 are surface relaxivity for T_1 and T_2, respectively; T_{1bulk} and T_{2bulk} are bulk longitudinal relaxation time and bulk transverse relaxation time, respectively. Additionally, S/V is pore surface-to-volume ratio, D is fluid diffusion coefficient, γ is the gyromagnetic ratio of a hydrogen proton, and G is magnetic field-strength gradient. T_2 distributions can be transformed into pore-size distributions when diffusion and bulk relaxations are neglected (Kenyon, 1997).

1.2 MOTIVATION

Conventional NMR log interpretations are based on T_2 distributions. An example of NMR T_2 distributions are presented on Track 7 in **Figure 1.2**. Many bimodal and trimodal distributions were observed, but one cannot determine whether these peaks are water or hydrocarbon because they can blend each other. Also, the T_2 cutoff line of 33 milliseconds cannot differentiate bound fluids from movable fluids. Klein and Martin (1997) proposed a variation of T_2 cutoff with capillary pressure to quantify core saturations. However, when core samples are not available or capillary pressure experiments are not reliable, numerical simulations are essential to estimate fluid saturations.

Many methods to calculate fluid saturation derived from different logging measurements were compared (Belgaised et al., 2004). Using AT90, the deepest array induction resistivity and other conventional logs, fluid saturation values were calculated, as shown on Track 9 of **Figure 1.2**: from right to left, gray is bound water, light blue is free water, green is oil, and red is gas. **Figure 1.3** compares NMR T_2 inversion results to

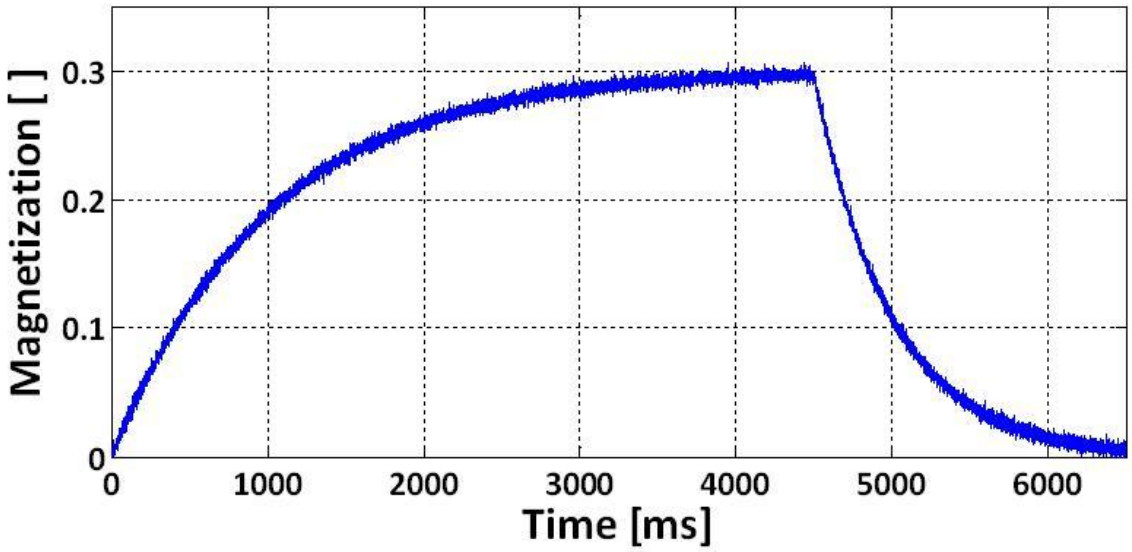

Figure 1.1: Graphical description of the NMR measurement cycle. The first step is a polarization of hydrogen nuclei called longitudinal relaxation. The second step is a decay of magnetization known as transverse relaxation. Both longitudinal and transverse relaxations include noise due to signal to noise ratio (SNR) in reservoir environments.

NMR T_2 simulation results using these saturation values**.** They do not agree because the calculated fluid saturations were incorrect. This is because original in-situ fluid saturations differ from fluid saturations in the presence of mud-filtrate invasion.

Another problem observed in this example is that gas and water signals blend in T_2 spectra. This is a very common phenomenon that makes fluid typing ambiguous. Instead of using conventional NMR T_2 distribution, 2D NMR data was used because it is suitable in distinguishing between two fluids. Fluid identification is based on the contrasts between two fluid properties. Multi-dimensional data can improve the diagnosis and assessment of saturating fluids (Sun and Dunn, 2005).

Numerical simulations are required to observe fluid signature changes on 2D NMR maps for different conditions. Minh et al. (2003) briefly explained how fluid signatures vary from their theoretical correlation lines. However, reservoir environments have various temperatures, wettabilities, lithologies, and pore sizes, and their surface-to-volume ratios can cause fluid signatures to differ from those of theoretical cases. Different sequence parameters used in NMR logging tools such as *TE*, *TW*, and *G* also affect NMR responses on 2D maps. Moreover, NMR responses from kerogen or heavy oil in unconventional reservoir show abnormal signatures. To overcome these challenges, algorithms to simulate NMR response based on petrophysical assumptions, mathematical equations, and NMR physics are imperative.

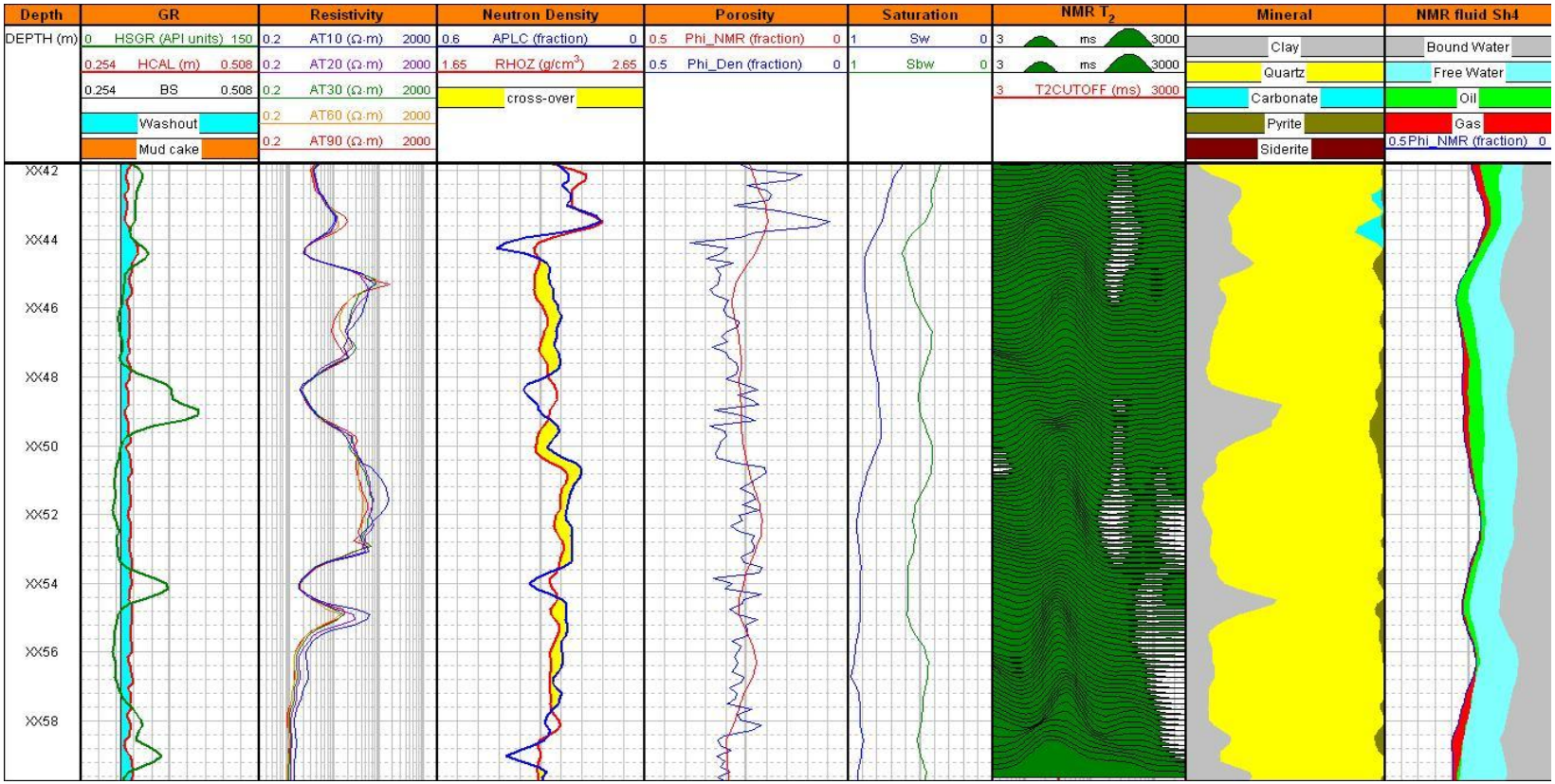

Figure 1.2: NMR T_2 distribution example: NMR T_2 distribution cannot differentiate movable fluid from bound water. Track 1: depth. Track 2: Gamma-Ray log, bit size, caliper log, washouts, and mud cake thickness. Track 3: apparent resistivity logs. Track 4: bulk density and neutron porosity calibrated in sandstone porosity units and their corss-over. Track 5: NMR porosity and density porosity. Track 6: calculated water saturation and irreducible water saturation. Track 7: NMR T_2 distribution and T_2 cutoff at 33 milliseconds. Track 8: Elemental Capture Spectroscopy (ECS) mineralogy data with clay, quartz, carbonate, pyrite, and siderite volumetric concentrations. Track 9: fluid saturations for bound water, free water, oil, and gas.

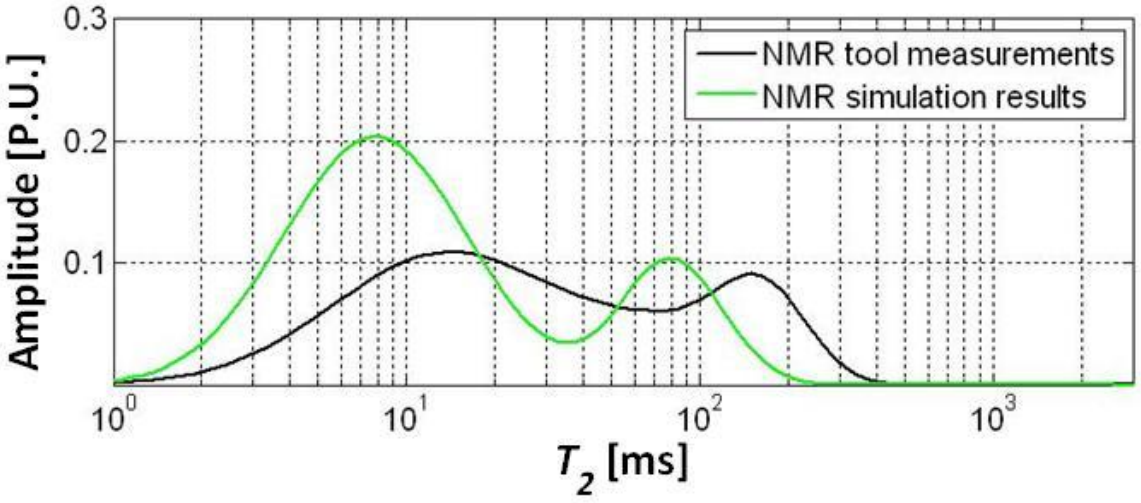

Figure 1.3: Comparison of NMR T_2 simulation results to measurements acquired at the depth of XX57 meters. NMR T_2 distributions from inversion results are in black and those from simulation results are in green. The NMR T_2 simulation result does not agree with field data because the calculated fluid saturations used for this simulation are incorrect. The discrepancy is due to the alteration of in-situ fluid saturations caused by mud-filtrate invasion.

1.3 RESEARCH OBJECTIVES

The major objective of this thesis is to introduce a workflow that accomplishes invasion-consistent interpretations of magnetic resonance measurements. **Figure 1.4** shows the general workflow diagram described in this thesis. NMR logging tools are susceptible to mud-filtrate invasions because they have shorter radial depths of investigation than those of resistivity and nuclear logging tools. This shallow sensing characteristic indicates that interpretations from NMR measurements can be influenced by drilling mud-filtrate invasion. Virgin fluids in the reservoir will be displaced away from the wellbore by the mud-filtrate, whereby the corresponding NMR response will be

masked by the invading fluid. Thus, water, oil, and gas saturation profiles may be a function of radial length from the wellbore.

It is well documented that NMR interpretation needs to take into account the mud-filtrate invasion process. In this case, the best way to produce a reliable interpretation is to construct a self-consistent reservoir model that agrees with available well logs and petrophysical properties. This can be done accurately by implementing the concept of the common stratigraphic framework (CSF) implemented by The University of Texas at Austin Petrophysics and Well-Log Simulator (UTAPWeLS) software. This method requires correct geological information to construct a petrophysical multi-layer earth model. Through this earth model, various petrophysical properties can be estimated by performing static and dynamic simulations. A robust earth model yields static and dynamic simulations that reproduce the available well logs. In addition, the spatial distribution of water, oil, and gas saturations obtained from the dynamic simulation can be used to quantify volume of mud-filtrate invasion at radial depths of interest. Reliable interpretation of NMR measurements using accurate fluid saturations in the invaded zone is the primary objective of this thesis. To reduce ambiguity of fluid typing, 2D NMR maps of D-T_1, D-T_2, and T_1-T_2 were simulated.

1.4 THESIS OUTLINE

Following this introductory chapter, the thesis consists of six additional chapters. Chapter 2 describes the geological information for the well β studied in this research. It describes constructions of static and dynamic reservoir models with petrophysical properties and agreements of simulated logs to measured logs verify these constructed models. Chapter 3 introduces petrophysical assumptions and mathematical equations to

develop algorithms to simulate NMR measurements. Chapter 4 provides various synthetic simulation results using these algorithms to validate the NMR physics. In chapter 5, these simulations are applied to two field cases and compare 2D NMR simulation results with inversion results. Chapter 6 introduces forward modeling and inversion to analyze 2D proton density distribution functions. Finally, chapter 7 gives conclusions and recommendations for future work.

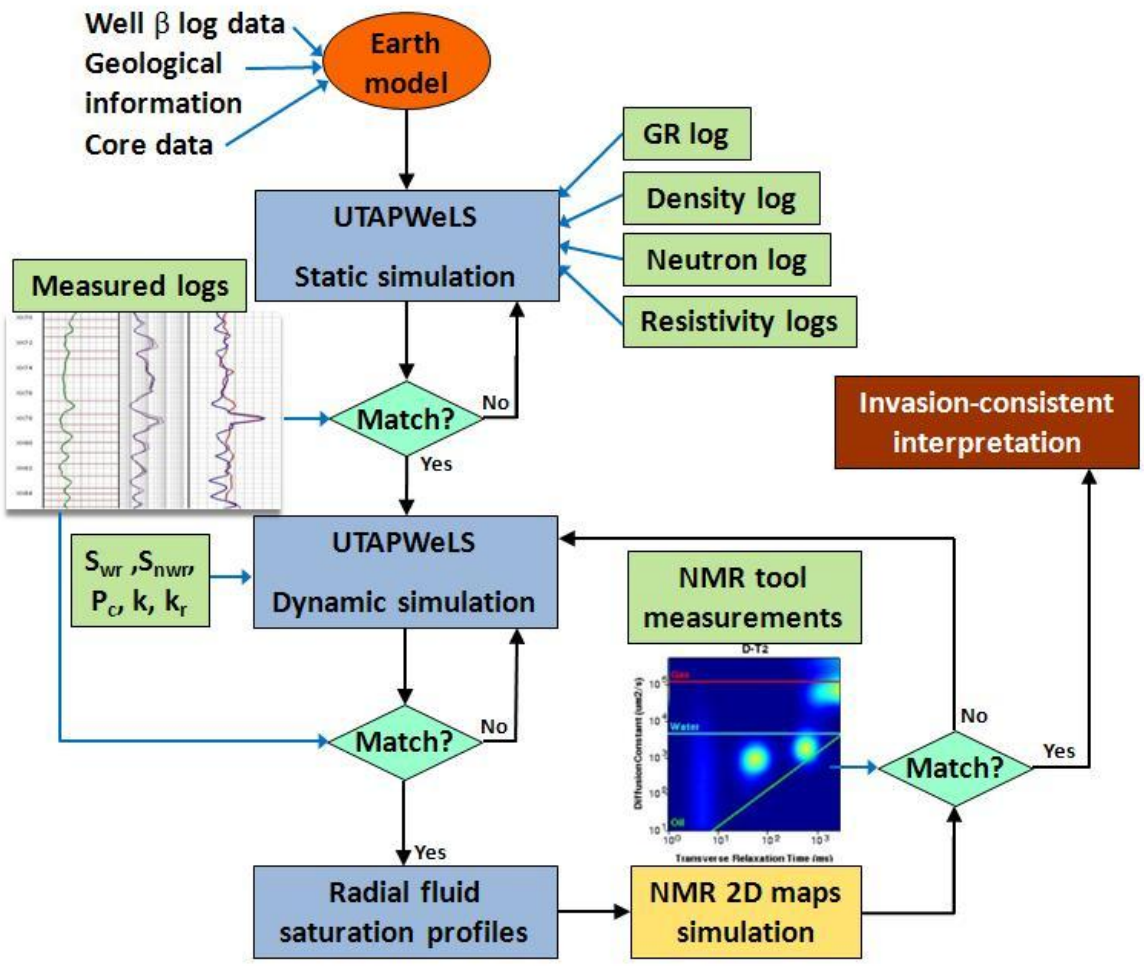

Figure 1.4: Workflow showing the sequential steps to interpret NMR measurements as affected by mud-filtrate invasion. The construction of a multi-layer static model requires a GR log, a density log, a neutron log, and five resistivity logs. Dynamic simulation needs wetting and non-wetting phase saturations, capillary pressure, absolute permeability, and relative permeability. The 2D NMR map simulations use the petrophysical parameters and saturation values from radial fluid saturation profiles.

Chapter 2: Construction of Reservoir Models

This chapter describes the constructing of static and dynamic reservoir models using the well β log data. Available logs include Gamma-Ray, apparent resistivity, nuclear, Elemental Capture Spectroscopy (ECS), and NMR.

2.1 Reservoir Description

Well β analyzed in this research is a siliciclastic formation with low to medium shale content. Dominant fluids in the area are gas and gas condensate. Structure is assembled by a two-way fold between steep extensional faults that are more than 200 meters long. Well β was sited in a variety of depositional environments, including levee/sheets, channel sands, and incised valley cuts. Main targets were levee/sheets piled across the top of the structure. There was also minor faulting considered to be sealing. This stratigraphic complexity increases the likelihood of numerous isolated compartments (Steene et al., 2012).

Presence of Clay (49.6 wt. %), Quartz (42.8 wt. %), carbonate (3.2 wt. %), pyrite (2.3 wt. %), and siderite (2.1 wt. %) has been reported in Elemental Capture Spectroscopy (ECS) mineralogic information. Additional to conventional well logs, Schlumberger MR Scanner tool provides NMR data. The effect of paramagnetic minerals on electrical resistivity and NMR measurements was negligible due to the small amount of pyrite in the formation. However, most well logs, including NMR measurements, were influenced by mud-filtrate invasion because of the shallow depth of investigation. Hence, integration of these measurements and mud-filtrate invasion plays a significant role in quantifying fluid types and distributions.

2.2 STATIC MULTI-LAYER MODELS

Petrophysical interpretation of well β begins with the construction of a reliable earth model. In order to construct petrophysical layer-by-layer models, applying the concept of CSF is essential. Bed boundaries were chosen based on the electrical resistivity and Gamma-Ray logs using The University of Texas at Austin's Petrophysical and Well Log Simulator (UTAPWeLS). The petrophysical calculator in UTAPWeLS computes the temperature, water resistivity, and volumetric shale concentrations.

Estimation of the volumetric shale concentration from Gamma-Ray logs was calculated using Clavier's method (Clavier et al., 1984). Shale correction for density porosity and neutron porosity was performed using this volumetric shale concentration. Inputs for the model include temperature, pressure, salinity, and composition and concentration of each fluid, mineral, and shale corresponding to petrophysical layers. **Figure 2.1** shows one example of a mineral and fluid composition table.

Subsequently, numerical resistivity log simulations were executed to quantify resistivity values from the constructed static model. From among others tested—Archie, Dual Water, Indonesia, Juhasz, and Waxman-Smits models—the Simandoux water saturation model (Simandoux, 1963) was selected to calculate apparent resistivity because of partially dispersed shale. The nuclear logs simulator can reproduce Gamma-Ray, neutron porosity, density porosity, and photoelectric factor (PEF). Simulation results for PEF were excluded because of its bias, which is thought to be due to the barite contained in mud filtrate. Electrical resistivity logs and nuclear logs simulation results are shown in **Figure 2.2**. General agreement between measurement logs and simulated logs indicates that static model simulation honors available well logs. The small discrepancy shown on the neutron and density plot is due to the absence of mud-filtrate invasion, which will be explained in Chapter 3.

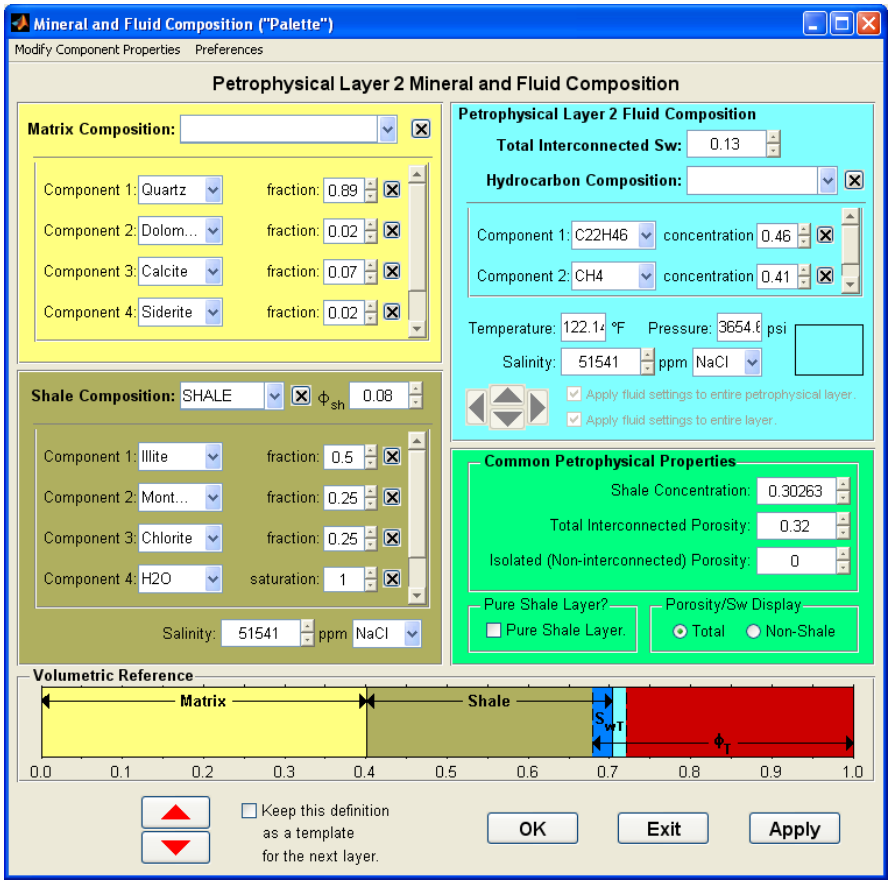

Figure 2.1: Mineral and fluid compositions for petrophysical layers. The user must assign matrix compositions and concentrations, shale compositions and concentrations, saturating fluid compositions and concentrations, and other petrophysical parameters such as porosity, salinity, and temperature to all the layers to simulate apparent resistivities and nuclear logs. Within a single layer, salinity and water saturation may vary in the radial direction. Volumetric reference summarizes the relative proportions of each input.

Variable	Value	Units
Archie's constant, a	1	[ ]
Archie's porosity exponent, m	2	[ ]
Archie's saturation exponent, n	2	[ ]
Resistivity of shale, R_{sh}	0.65	[Ohm-m]
Connate water resistivity at formation temperature, R_w	0.08	[Ohm-m]

Table 2.1: Summary of assumed parameters for Simandoux water saturation model. These parameters were chosen to simulate resistivity logs that exhibit the best matches to measured resistivity logs.

Variable	Value	Units
Density of Illite, ρ_{Illite}	0.78	[g/cc]
Density of Montmorillonite, $\rho_{Montmorillonite}$	2.63	[g/cc]
Density of Chlorite, $\rho_{Chlorite}$	2.65	[g/cc]
Density of Quartz, ρ_{Quartz}	2.65	[g/cc]
Density of Dolomite, $\rho_{Dolomite}$	2.87	[g/cc]
Density of Calcite, $\rho_{Calcite}$	2.71	[g/cc]
Density of Siderite, $\rho_{Siderite}$	3.96	[g/cc]
Density of Pyrite, ρ_{pyrite}	5.01	[g/cc]

Table 2.2: Assumed mineral densities for static model construction.

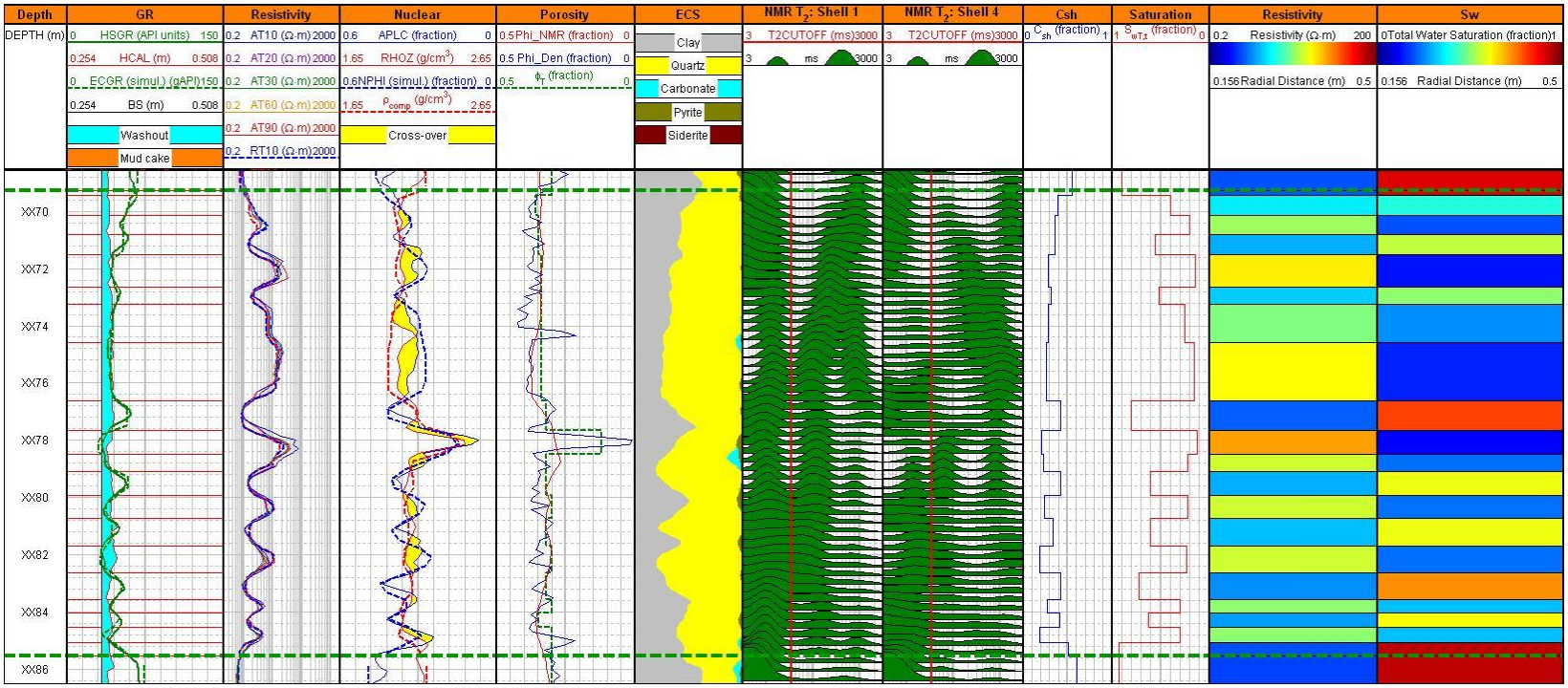

Figure 2.2: Calculated static model along the depth interval of interest. Numerically simulated Gamma-Ray logs, apparent resistivity logs, and nuclear logs are marked as dashed lines. Track 1: depth. Track 2: numerically simulated and measured Gamma-Ray logs, bit size, caliper log, washouts, and mud cake thickness. Track 3: numerically simulated and measured apparent resistivity logs. Track 4: numerically simulated and measured bulk density and neutron porosity calibrated in sandstone porosity units and their corssover. Track 5: NMR porosity, density porosity, and earth model porosity. Track 6: ECS mineralogy data with clay, quartz, carbonate, pyrite, and siderite. Track 7: T_2 distributions measured at 1.5 inches from the borehole. Track 8: T_2 distributions measured at 2.7 inches from the borehole. Track 9: calculated volumetric shale concentration. Track 10: calculated water saturation. Track 11: spatial distribution of resistivity. Track 12: spatial distribution of water saturation.

2.3 DYNAMIC MULTI-LAYER MODELS

Once the static model calculations have been completed, a dynamic reservoir model can be constructed that honors the physics of mud-filtrate invasion. Numerical simulation settings with various dynamic petrophysical properties must be input into the fluid flow simulator. These include fluids properties such as viscosity, density, salinity, and temperature. Also needed are drilling variables, including type of mud, mud cake porosity and permeability, time of invasion, and overbalance pressure. Relative permeability and capillary pressure for each layer is calculated based on Brooks-Corey model parameters (Brooks and Corey, 1966).

In permeable porous media such as reservoir rocks, mud-filtrate invasion takes place during the drilling process. OBM displaces in-situ formation fluids in well β because of the pressure difference between borehole and formation. The mud weight is relatively high (11.3 lb/gal). Invasion length is determined by various petrophysical parameters, including reservoir porosity, permeability, overbalanced pressure, viscosity of mud, and time of invasion. Two-phase immiscible fluid flow, cylindrical flow, and permeability isotropy are assumed in the numerical simulation of mud-filtrate invasion (George, 2003) using UTAPWeLS.

Due to the difference between the density and hydrogen index (HI) of the OBM and formation gas, both neutron porosity and bulk density increased, and the cross-over between them decreased. **Figure 2.3** shows numerical simulations that correctly reproduced neutron porosity, Gamma-Ray, electrical resistivity, and bulk density logs estimated at the zone of interest. After ascertaining that all simulated logs agreed with measured logs, radial fluid saturation profiles were plotted, as will be discussed in

Chapter 5. Saturation values at approximately 1.5 inches and 2.7 inches into the formation were selected for numerical NMR simulations.

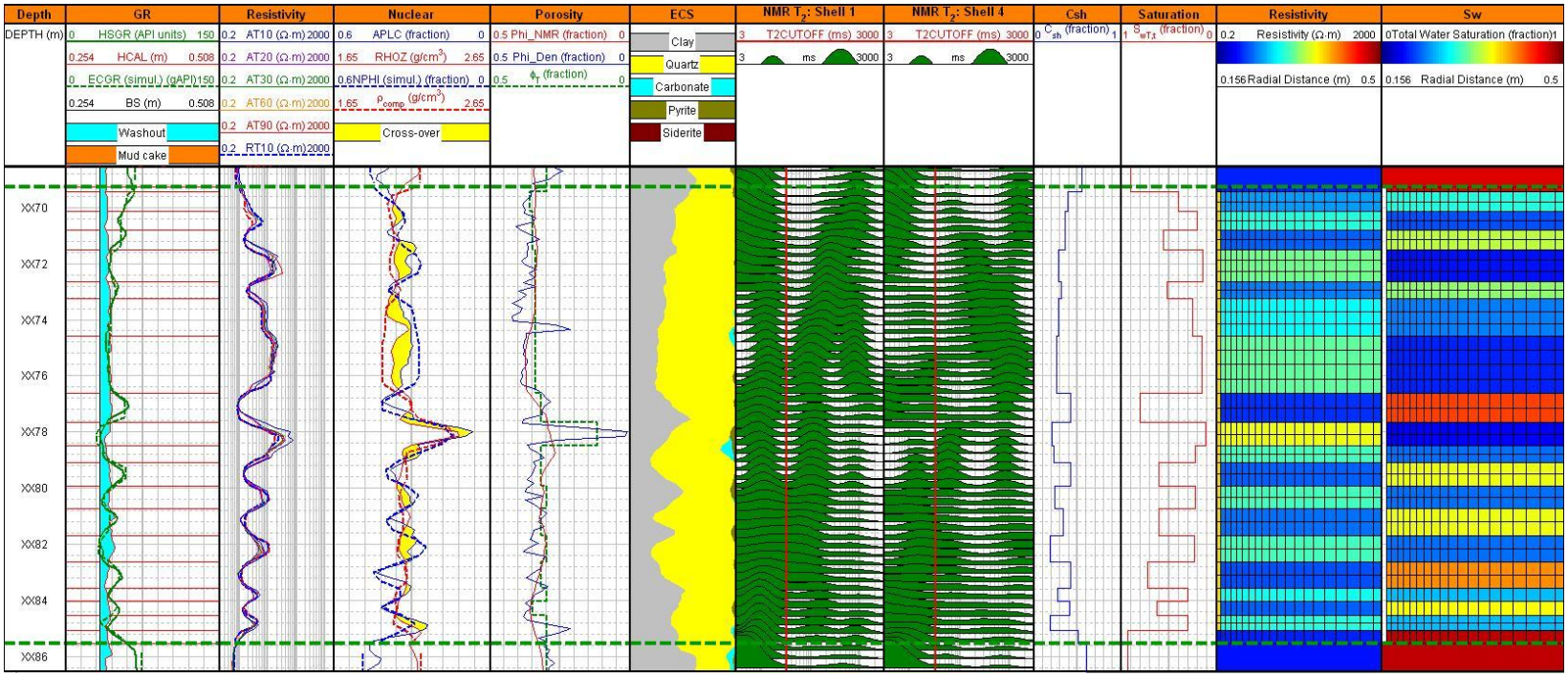

Figure 2.3: The final multi-layer dynamic model with the simulation of mud-filtrate invasion. Track 1: depth. Track 2: numerically simulated and measured Gamma-Ray log, bit size, caliper log, washouts, and mud cake thickness. Track 3: numerically simulated and measured apparent resistivity logs. Track 4: numerically simulated and measured bulk density and neutron porosity calibrated in sandstone porosity units and their corssover. Track 5: NMR porosity, density porosity, and earth model porosity. Track 6: ECS mineralogy data with clay, quartz, carbonate, pyrite, and siderite. Track 7: T_2 distributions measured at 1.5 inches from the borehole. Track 8: T_2 distributions measured at 2.7 inches from the borehole. Track 9: calculated volumetric shale concentration. Track 10: calculated water saturation. Track 11: spatial distribution of resistivity. Track 12: spatial distribution of water saturation.

Chapter 3: Development of Multi-Dimensional NMR Simulations

Multi-dimensional NMR simulation algorithms were developed to cross-validate the mud-filtrate invasion process. Using parameters and saturation values from UTAPWeLS, these algorithms provide 2D maps of D-T_1, D-T_2, and T_1-T_2 at different depths of investigations.

3.1 Petrophysical Assumptions

The principal assumption for these algorithms is that all pores have perfect spherical shapes, which have the smallest surface volume ratio per unit volume. These pores contain many kinds of fluids, but only water contacts the surface of grains. Relaxivity of the surface between two fluids was neglected because it is much smaller than that between a fluid and a grain surface. Also, Gaussian-log distributions of pore size, diffusion coefficient and T_{2bulk} were assumed. Because fluid types and pore geometries affect T_2 distributions (Toumelin and Torres-Verdín, 2002), the model was simplified so that there are two different pore sizes: smaller pores contain bound water, whereas bigger pores contain free water, oil, and gas.

3.2 Mathematical Models

We assumed perfectly spherical pores, so equations (1.1) and (1.2) can be modified as

$$\frac{1}{T_1} = \frac{1}{T_{1bulk}} + \rho_1 \frac{3}{r}, \tag{3.1}$$

and

$$\frac{1}{T_2} = \frac{1}{T_{2bulk}} + 3\frac{\rho_2}{r} + \frac{D(\gamma GTE)^2}{12}, \tag{3.2}$$

where r represents radius of the pores. The equation (3.2) can be rearranged as in radius form:

$$r = \frac{3\rho_2}{\left(\frac{1}{T_2} - \frac{1}{T_{2bulk}} - \frac{D(\gamma GTE)^2}{12}\right)} \tag{3.3}$$

The final equation for water is expressed as an integral form of $P_{pores}(R_2(T_2),D)$• $R_2'(T_2,D)$ weighted with the density function of T_{2bulk} decays, $S(T_{2bulk})$.:

$$G_{2water}(T_2, D) = N \int_{-\infty}^{\infty} P_{pores}[R_2(T_2), D] R_2^{'}(T_2, D) S(T_{2bulk}) dT_{2bulk}, \tag{3.4}$$

where pore size distribution, derivative of pore size, and density function of T_{2bulk} can be expressed as

$$P_{pores}(R_2(T_2), D) = \mathrm{e}^{-\frac{\left(\log\frac{3\rho}{\left(\frac{1}{T_2} - \frac{1}{T_{2bulk}} - \frac{(\gamma GTE)^2 D_{water}}{12}\right)} - \log(\mu)\right)^2}{2\sigma^2}}, \tag{3.5}$$

$$R_2^{'}(T_2, D) = \frac{3\rho\, T_{2bulk}^2}{\left(T_{2bulk} - T_2 - \frac{(\gamma GTE)^2 D_{water}}{12} T_{2bulk} T_2\right)^2}, \tag{3.6}$$

and

$$S(T_{2bulk}) = \mathrm{e}^{-\frac{\log T_2 - \log T_{2bulk}}{2\sigma_{shell}}^2}, \tag{3.7}$$

where σ_{shell} is standard deviation of T_2 distribution of fluid in shell, respectively.

Oil and gas distributions can be calculated in the same manner; however, surface relaxivity terms are excluded because the formation is assumed to be water-wet.

$$G_{2oil}(T_{2bulk}, D) = \left(\frac{1}{1 - T_2 \frac{(\gamma GTE)^2 D_{oil}}{12}} \right) \mathrm{e}^{-\frac{\left[\log\left(\frac{1}{\frac{1}{T_2} - \frac{(\gamma GTE)^2 D_{oil}}{12}} \right) - \log(T_{2bulk}) \right]^2}{2\sigma_{core}^2}} \tag{3.8}$$

$$G_{2gas}(T_{2bulk}, D) = \left(\frac{1}{1 - T_2 \frac{(\gamma GTE)^2 D_{gas}}{12}} \right) \mathrm{e}^{-\frac{\left[\log\left(\frac{1}{\frac{1}{T_2} - \frac{(\gamma GTE)^2 D_{gas}}{12}} \right) - \log(T_{2bulk}) \right]^2}{2\sigma_{core}^2}} \tag{3.9}$$

For the above equations, diffusion coefficients for water, oil, and gas are expressed as a Gaussian distribution:

$$D_{water} = \mathrm{e}^{-\frac{\log D_i - \log D_w}{2\sigma_{Dw}}^2}, \quad D_{oil} = \mathrm{e}^{-\frac{\log D_i - \log D_o}{2\sigma_{Do}}^2}, \text{ and } D_{gas} = \mathrm{e}^{-\frac{\log D_i - \log D_g}{2\sigma_{Dg}}^2}.$$

Equations for T_1 can be calculated the same way, but without diffusion relaxation terms. Then the total T_1 and T_2 distributions are summations of each fluid weighted by the corresponding saturation and the hydrogen index, i.e.,

$$T_{1total} = \underbrace{HI_{water} S_{bw} G_{2bw}(T_{1bulk}, D)}_{bound\ water} + \underbrace{HI_{water} S_{fw} G_{2\,fw}(T_{1bulk}, D)}_{free\ water} + \underbrace{HI_{oil} S_{oil} G_{2oil}(T_{1bulk}, D)}_{oil} + \underbrace{HI_{gas} S_{gas} G_{2gas}(T_{1bulk}, D)}_{gas}, \quad (3.10)$$

and

$$T_{2total} = \underbrace{HI_{water} S_{bw} G_{2bw}(T_{2bulk}, D)}_{bound\ water} + \underbrace{HI_{water} S_{fw} G_{2\,fw}(T_{2bulk}, D)}_{free\ water} + \underbrace{HI_{oil} S_{oil} G_{2oil}(T_{2bulk}, D)}_{oil} + \underbrace{HI_{gas} S_{gas} G_{2gas}(T_{2bulk}, D)}_{gas}, \quad (3.11)$$

where HI_{water}, HI_{oil}, and HI_{gas} are the hydrogen index for water, oil, and gas, respectively and S_{bw}, S_{fw}, S_{oil}, and S_{gas} are the saturation of bound water, free water, oil, and gas, respectively. The sum of saturations should be 1 because of the material balance equation.

Chapter 4: Synthetic Case: 2D NMR Simulations

This chapter introduces several synthetic cases to verify the reliability and accuracy of the 2D NMR map simulations. Here I will demonstrate how several NMR parameters affect fluid signature changes observed on 2D maps and that these simulations honor NMR physics. An analysis of wettability changes from strong water-wet to oil-wet will be presented, and the NMR response of kerogen in nano-scale pores will be discussed.

4.1 The Effect of Various NMR Parameters

The objective of this section is to observe NMR responses in 2D maps according to changes of NMR parameters. **Figure 4.1** is a synthetic example of NMR D-T_1, D-T_2, and T_1-T_2 maps. All parameters used to generate this result are shown in **Table 4.1**. For simplicity, two distinct fluid signatures are considered, bound water and gas of 50% saturation.

First, the parameter of surface relaxivity varies according to mineral composition. In carbonate formation, lengthened T_1 and T_2 water signatures can be observed due to carbonate's low surface relaxivity. Gas signatures remain the same because gas is not in contact with grains. The NMR response of long inter-echo time leads to slightly shortened gas signatures because diffusion coefficient of the gas is relatively larger than that of other fluids. The strength of each fluid signature represents different magnetization of each fluid. Dual-*TW* measurements make different polarizations for each fluid. Comparing the 99% polarized water seen both when the *TW* is 45,000 ms and *TW* is 13,000 ms, gas signatures are polarized only about 63% in the shorter *TW* case. The effect of the increased magnetic field gradient is prominent for the gas signal. Even

though the increased value of the diffusion term shortened T_2 of water and gas, the shortened time of water is negligible. This is because the dominating term contributing T_2 for water is not a diffusion term but a surface relaxation term. With larger pore sizes, only the water signatures lengthened because gas is not in contact with grains. Given different pore geometries, pore shape can be changed from a perfect sphere to a cube. The surface-to-volume ratio will be increased because a sphere has the smallest surface volume ratio for unit volume. The increased value of the surface relaxation term leads to shortened T_1 and T_2. Theoretically, the increased temperature induces the increased diffusion coefficient, T_{1bulk} and T_{2bulk} (Bloembergen et al., 1947). But the effects of the formation temperature on T_{2bulk} and the diffusion coefficient are so small that the NMR response in the high-temperature case and the low-temperature case could not be distinguished. Gas density also depends on temperature and pressure, but it was neglected in these cases.

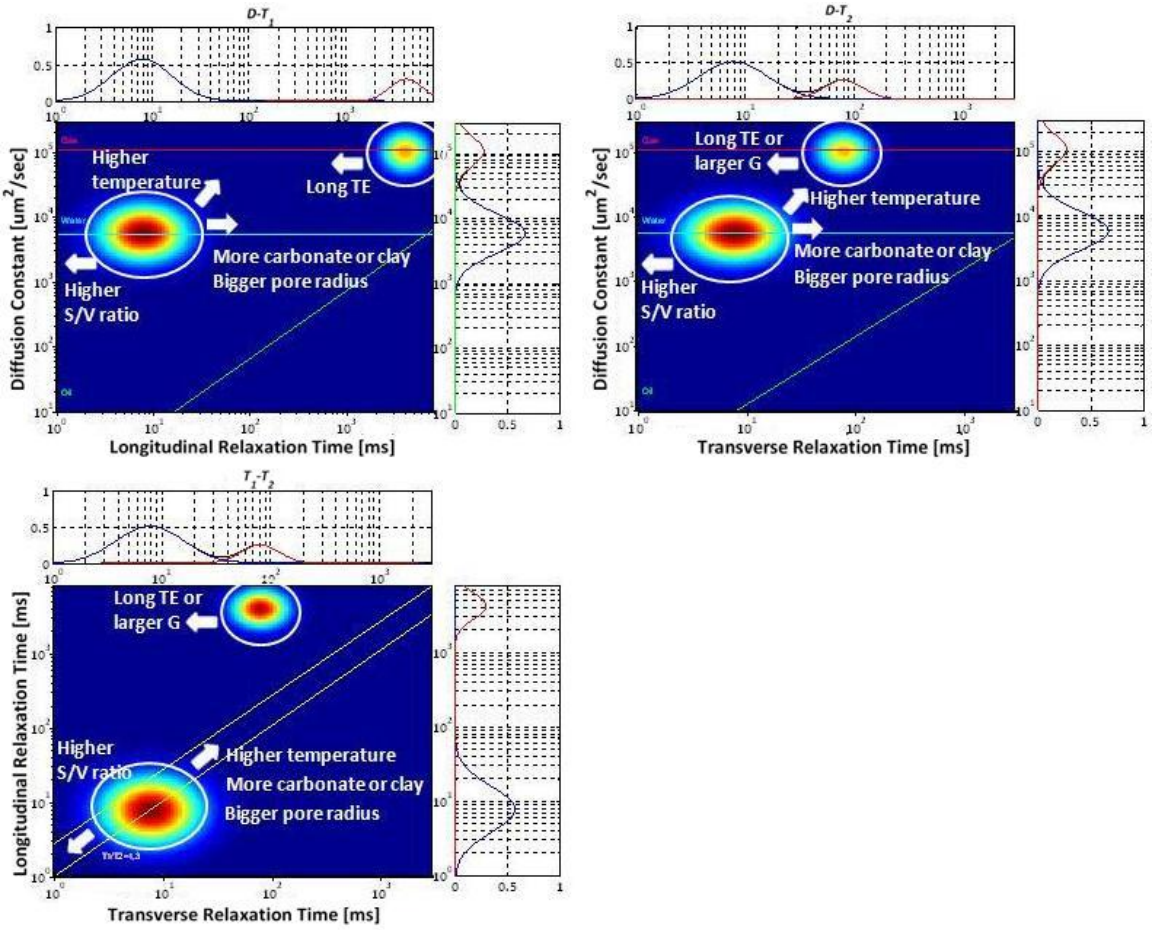

Figure 4.1: Summary of the NMR response in D-T_1, D-T_2, and T_1-T_2 maps for synthetic cases. Long inter-echo time or stronger magnetic gradient moves the gas signatures in the left-arrow direction. Larger pore radius or lithology changes from siliciclastic to carbonate make the smaller surface relaxation that causes the wetting fluid signatures to move in the other direction, as indicated by the right arrow. Higher temperature increases both relaxation times and diffusion constants of liquid. Higher surface to volume ratio per unit volume causes wetting fluids signatures to shift to shortened relaxation times.

Variable	Value	Units
Hydrogen Index of water, HI_w	1	[ ]
Hydrogen Index of oil, HI_o	0.938	[ ]
Hydrogen Index of gas, HI_g	0.338	[ ]
Hydrogen Index of OBM, HI_{OBM}	0.9	[ ]
Diffusion constant of water, D_w	5000	[um^2/sec]
Diffusion constant of light oil, $D_{lightoil}$	1500	[um^2/sec]
Diffusion constant of gas, D_{gas}	70000	[um^2/sec]
Diffusion constant of OBM, D_{OBM}	10 to 3000	[um^2/sec]
Surface relaxivity of sand, ρ_{sand}	30	[um/sec]
Surface relaxivity of carbonate, $\rho_{carbonate}$	1.5	[um/sec]
Surface relaxivity of clay, ρ_{clay}	2 to 5	[um/sec]
Surface relaxivity of etc. , ρ_{etc}	2 to 10	[um/sec]
Bulk relaxation time of water, T_{2bulk_water}	3000	[ms]
Bulk relaxation time of water, T_{2bulk_oil}	1500	[ms]
Bulk relaxation time of water, T_{2bulk_gas}	4500	[ms]
Bulk relaxation time of water, T_{2bulk_OBM}	150	[ms]
Inter-echo time, TE	0.45	[ms]
Polarization time, TW	13000	[ms]
Magnetic gradient, G	15	[Gauss/cm]

Table 4.1: Summary of petrophysical properties assumed in the synthetic 2D NMR simulations. Diffusion constant of OBM varies because it is a mixture of several fluids.

4.2 THE EFFECT OF WETTABILITY

All the previous examples assumed a perfect water-wet formation, with a wettability of one. Although there are many exceptions, carbonates reservoirs are known as oil-wet to neutral, whereas sandstone reservoirs are often neutral to water-wet. However, there are many circumstances in which reservoir wettability changes. When oil bubbles migrate from a source rock into the initially water saturated reservoir rock, oil bubbles enter into the relatively larger pores first, due to capillary forces. Thus the condition of the formation may be one in which the smaller pores remain water-filled, water-wet, whereas the larger pores may have become oil-wet. Aging and surfactants could also cause alteration from wettability to a more oil-wet character (Zhang et al., 2000). Hence, surface relaxation terms for water and oil must be updated according to the wettability index and water saturation, which depend on pore size (Looyestijn and Hofman, 2006). Equations (3.1) and (3.2) for water and oil become

$$\frac{1}{T_{1,w}} = \frac{1}{T_{1bulk,w}} + \rho_{1,w}\left(\frac{3}{r}\right)\frac{I_w(r)}{H_w(r)}, \tag{4.1}$$

$$\frac{1}{T_{2,w}} = \frac{1}{T_{2bulk,w}} + \rho_{2,w}\left(\frac{3}{r}\right)\frac{I_w(r)}{H_w(r)} + \frac{D(\gamma GTE)^2}{12}, \tag{4.2}$$

$$\frac{1}{T_{1,o}} = \frac{1}{T_{1bulk,o}} + \rho_{1,o}\left(\frac{3}{r}\right)\frac{1-I_w(r)}{1-H_w(r)}, \tag{4.3}$$

and

$$\frac{1}{T_{2,o}} = \frac{1}{T_{2bulk,o}} + \rho_{2,o}\left(\frac{3}{r}\right)\frac{1-I_w(r)}{1-H_w(r)} + \frac{D(\gamma GTE)^2}{12}, \tag{4.4}$$

where $I_w(r)$ and $H_w(r)$ are the wettability index and the water saturation function, respectively, that depend on pore size. An additional assumption for oil-wet cases is that gas remains a non-wetting phase. Since gas is not in contact with grains, gas signatures shown on both water-wet formations and oil-wet formations should be similar. Water-wet formations should have higher irreducible water saturation and less residual oil saturation. Also, oil-wet formations tend to have higher residual oil saturation and less irreducible water saturation (Chen et al., 2004).

When oil is in contact with the rock surface, it has a shorter NMR relaxation than bulk oil. **Figure 4.2** shows typical oil-wet reservoir NMR responses of water and oil signatures on 2D maps, with bound water, free water, and light oil of saturations as 0.3, 0.4, and 0.3 respectively. From these NMR simulation results, shortened NMR relaxation of oil and lengthened NMR relaxation of free water were observed as the wettability index decreased from one to zero. Longitudinal relaxation time for oil and water are similar to transverse relaxation time because diffusion relaxation terms for these fluids are relatively small. **Appendix** summarizes the both the Amott wettability index and the United States Bureau of Mines (USBM) wettability index.

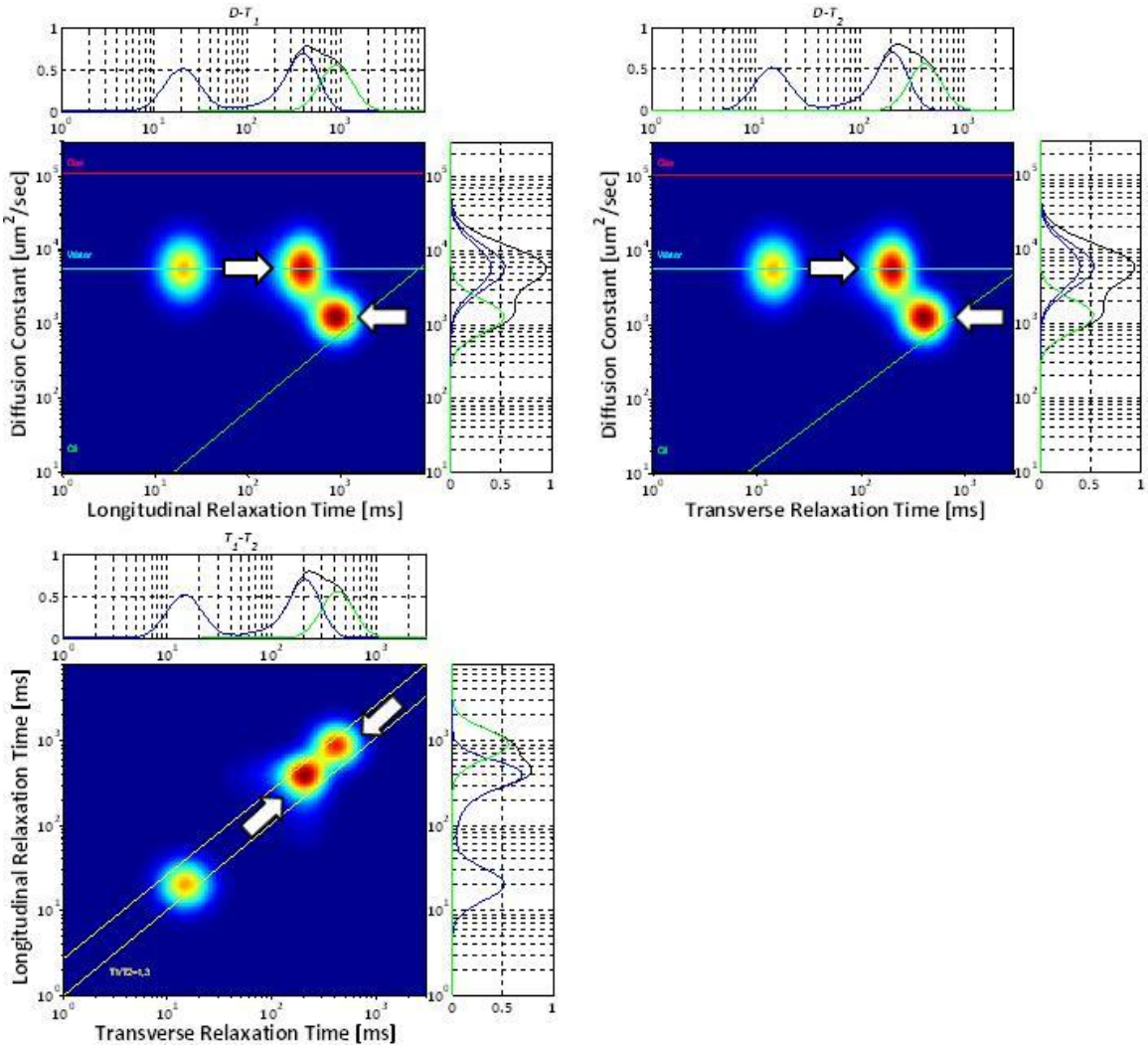

Figure 4.2: Summary of the NMR response in D-T_1, D-T_2, and T_1-T_2 maps for neutral to oil-wet case. As the formation wettability changes from water-wet to oil-wet, fewer water bubbles contact grains and their surface relaxation decreases. Subsequently, relaxation times of water signatures lengthened, as indicated by the right arrow. The contact with grains and oil bubbles, instead of with water bubbles, leads to shorter relaxation times of oil signatures.

4.3 EFFECT OF KEROGEN IN NANO-SCALE PORES

By definition, kerogen is a mixture of organic chemical compounds that make up a portion of the organic matter in sedimentary rocks. In order to estimate NMR responses in the formation containing kerogen, we need to know its environment. It is challenging for NMR tools to detect kerogen because it has both solid and liquid-like elements. In addition, due to its extremely small size, nano-scale pores in organic kerogen restrict diffusional motion and have very high surface volume ratios that enhance surface relaxation. In a high pressure environment, gas exists as an adsorbed phase on the pore surface and molecular exchange is continuous between the adsorbed and free phases. In some reservoirs, the NMR response from adsorbed gas can approach 40% of the total GIIP. Therefore, equations for T_1 and T_2 relaxation of gas must be modified according to the fraction of molecules in the adsorbed phase. ε is the fraction of molecules in the adsorbed phase and 1-ε is the fraction of non-adsorbed molecules in the pore interior. Then T_1 and T_2 equations can be described as

$$\frac{1}{T_{1,eff}} = \frac{1-\varepsilon}{T_{1,\,free}} + \frac{\varepsilon}{T_{1,adsorbed}}, \tag{4.5}$$

and

$$\frac{1}{T_{2,eff}} = \frac{1-\varepsilon}{T_{2,\,free}} + \frac{\varepsilon}{T_{2,adsorbed}}. \tag{4.6}$$

Interactions between adsorbed and free phase gas also affect the gas diffusion coefficient. Fickian diffusion occurs when the molecule-molecule collisions are dominant because the mean free path is smaller than the pore dimensions. Knudsen diffusion occurs when the molecule-surface collisions are dominant because the mean free path is larger

than the pore dimensions (Kausik et al., 2011). Thus, the effective diffusion coefficient could be described as

$$D_{eff} = (1-\varepsilon)D_{gas} + \varepsilon D_{ad} . \quad (4.7)$$

Figure 4.3 shows simulation results for kerogen in nano-scale pores. For simplicity, only two fluids of bound water and gas saturations of 0.6 and 0.4 were considered. The molecule fraction in the adsorbed phase was assumed to be 40%. In D-T_2 maps, faster relaxation modes and slower apparent diffusion coefficients for the confined gas molecules have been identified. Whereas liquid-like kerogen has a T_1/T_2 ratio of 1, solid kerogen has a larger T_1/T_2 ratio because of intramolecular dipolar coupling (Washburn and Birdwell, 2013). Bulk relaxation processes in the solid component and the dipolar coupling at the fluid-kerogen interface were not considered in the simulation because surface relaxation is dominant compared to bulk relaxation and diffusion relaxation. Due to extremely small pore sizes and very high surface volume ratio, T_1 and T_2 relaxation times were greatly shortened. Reduction in the gas diffusion coefficient is caused by restricted diffusion and surface adsorption. Due to the extremely small pore sizes, resulting fluid signatures overlapped on the relation times below 10 milliseconds. Distinguishing between adsorbed gas and free gas is very challenging. Thus, to obtain more accurate NMR field data, it is necessary to use a large number of echoes at short times.

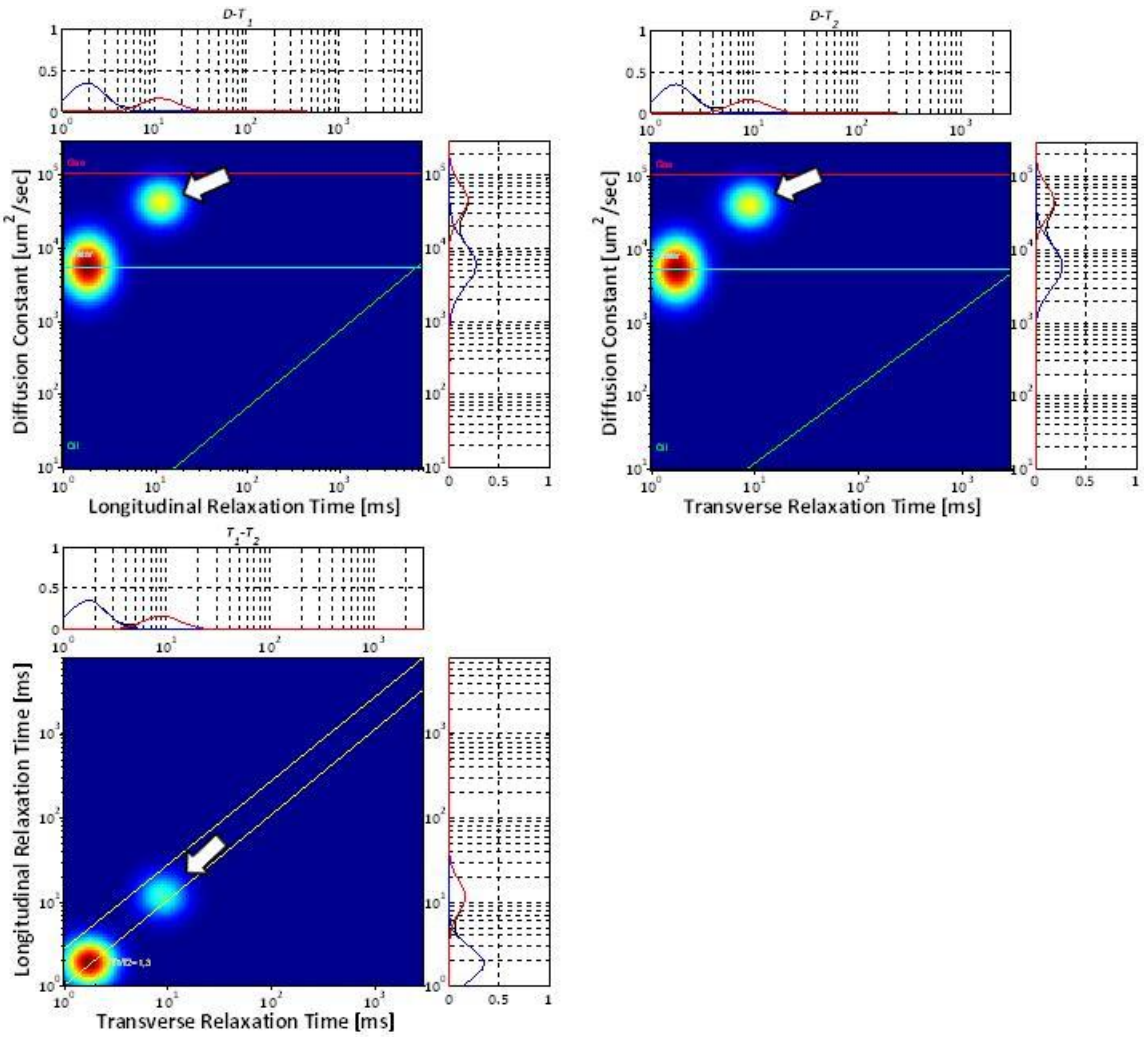

Figure 4.3: The synthetic case of the NMR responses in D-T_1, D-T_2, and T_1-T_2 maps for kerogen contained in nano-scale pores. Due to the extremely small pore sizes, relaxation times of all fluid signatures greatly decrease in the order of a few milliseconds. The effective diffusion coefficient of gas also decreases because of the continuous molecular exchange between free phase and adsorbed gas in kerogen.

Chapter 5: Field Cases: 2D NMR Simulations

This chapter analyzes various NMR 2D maps obtained from the inversion results and from the simulations performed with the algorithm developed in Chapter 3. The influence of mud-filtrate invasion on NMR responses is described with examples of oil- and gas-bearing sand and water-bearing sand at well β.

5.1 Field Case No. 1: Oil- and Gas-Bearing Siliciclastic Formation

Figure 5.1 shows the first field example on well β at the depth of interest. Low to medium Gamma-Ray log values indicates low shale concentration. High values of apparent resistivity logs provide evidence of hydrocarbon presence. Crossover between bulk density and nuclear porosity, which is calibrated in limestone porosity units, confirms presence of gas. Total porosity estimated with both NMR porosity and density porosity is about 30%. Bimodal and trimodal NMR T_2 distributions cannot guarantee the exact fluid typing because overlapping fluids cannot be distinguished from one another. The T_2 cutoff for NMR distributions is 33 milliseconds.

Figure 5.2 shows NMR inversion results at 1.5 inches from the borehole. Conventional NMR T_1 and T_2 distributions cannot differentiate light oil and gas signatures. However, multi-dimensional NMR maps can provide more accurate interpretations because they represent contrast in fluid diffusion coefficient. The D-T_1 and D-T_2 maps show theoretical water, oil, and gas correlation lines, and the T_1-T_2 maps reveal the one and three T_1/T_2 ratio lines. **Figure 5.3** gives the same NMR inversion results with the depth of investigation of 2.7 inches from the borehole.

Gas signatures appear within a range of long relaxation times (T_2 ~ 2000 ms) and high diffusion constants. Light oil signatures are detected above the oil correlation line

with long relaxation times and medium diffusion constants. OBM filtrate is clearly observed in the middle of the maps. Lo et al. (2002) showed mixing rules and correlations of NMR relaxation times with fluid properties of methane/hydrocarbon mixtures. Similarly, in **Figure 5.2**, the OBM signatures have increased in diffusion and decreased in relaxation time due to the dissolved in-situ gas.

The most distinct difference between the two maps is the OBM signatures found at the center. Since the mud-filtrate saturation gradually decreases when radial length from the wellbore increases, OBM signatures shown in **Figure 5.3** are smaller than those shown in **Figure 5.2**. The NMR response shown in **Figure 5.3** is still masked by mud-filtrate, but these OBM signatures are negligible. Smaller volumes of OBM and more in-situ fluids, in this case, the light oil and gas, were detected in **Figure 5.3** because the NMR response is farther from the borehole. Weak signatures ranging within low relaxation times are a mixture of bound water and mud solid invasion.

These NMR responses can be simulated with the algorithm discussed in Chapter 3. Petrophysical parameters acquired from static and dynamic simulations and fluid saturations (**Figure 5.4)** are needed as inputs. This invasion profile exhibits a smooth radial front of oil and gas saturations. **Table 5.1** reports fluid saturations at a distance of 1.5 inches and 2.7 inches from the wellbore. **Figure 5.5** and **Figure 5.6** show NMR D-T_1, D-T_2, and T_1-T_2 simulation results at corresponding depths of investigation. According to this simulation result, about 25% of movable virgin fluids were displaced by OBM at 1.5 inches away from the wellbore. Hence, based on the volume of OBM and in-situ fluids shown at different depths of investigation, simulation honors the physics of mud-filtrate invasion.

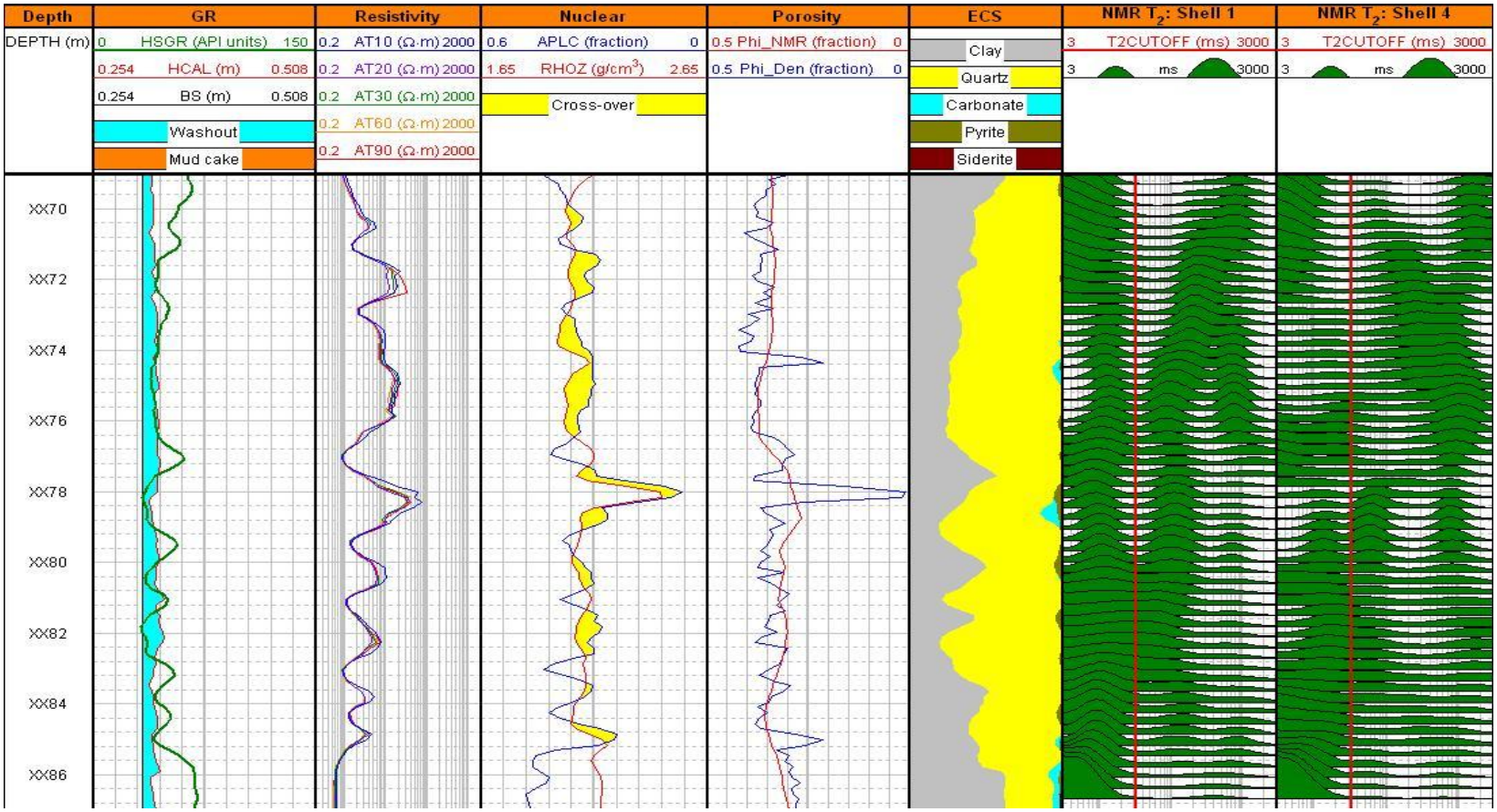

Figure 5.1: Field Case No. 1: Wireline logs along the depth interval of interest. Track 1: depth. Track 2: Gamma-Ray log, bit size, caliper log, washouts, and mud cake thickness. Track 3: apparent resistivity logs. Track 4: bulk density and neutron porosity calibrated in sandstone porosity units and their corssover. Track 5: NMR porosity and density porosity. Track 6: ECS mineralogy data with clay, quartz, carbonate, pyrite, and siderite. Track 7: T_2 distributions measured at 1.5 inches from the borehole. Track 8: T_2 distributions measured at 2.7 inches from the borehole.

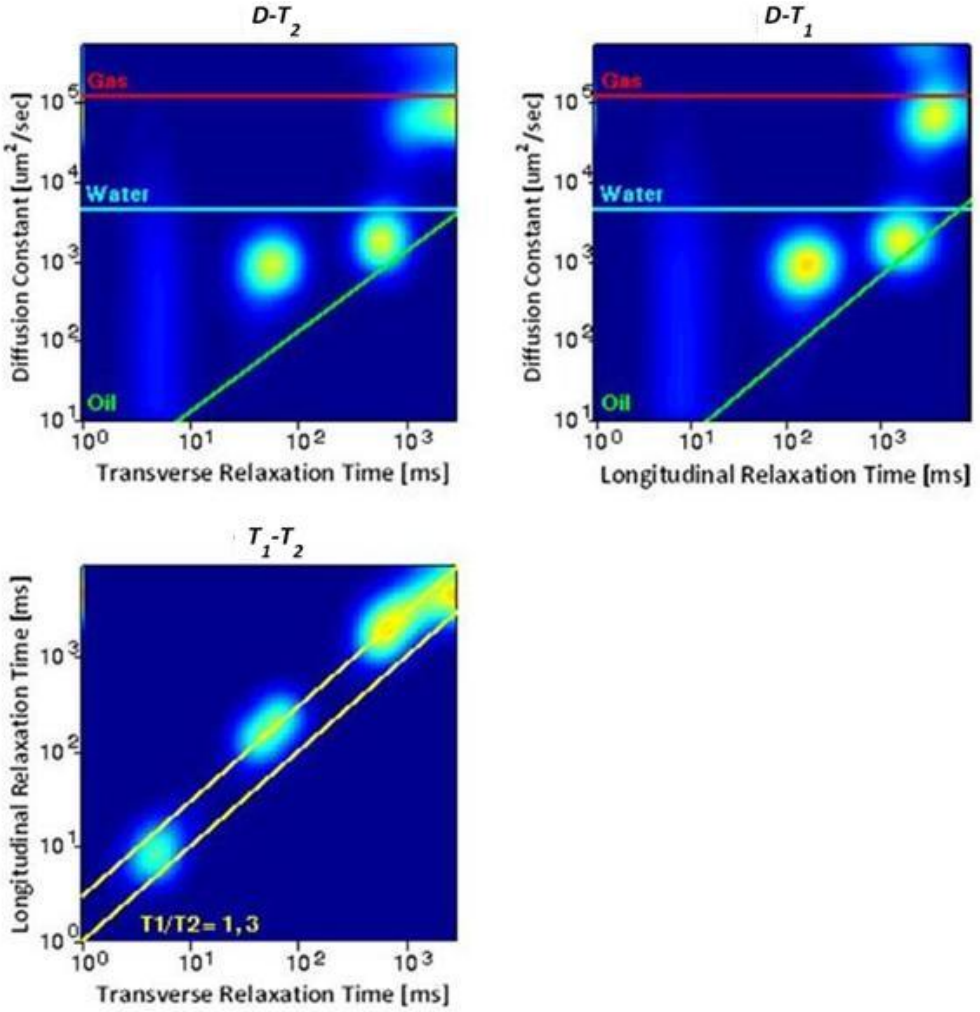

Figure 5.2: Field Case No. 1: D-T_1, D-T_2, and T_1-T_2 maps from NMR inversion results for the depth interval XX75-XX76 meters with a radial length of 1.5 inches from the borehole. From these maps, four explicit fluid signatures can be identified. These are gas, light oil, OBM, and a mixture of bound water and mud solid invasion.

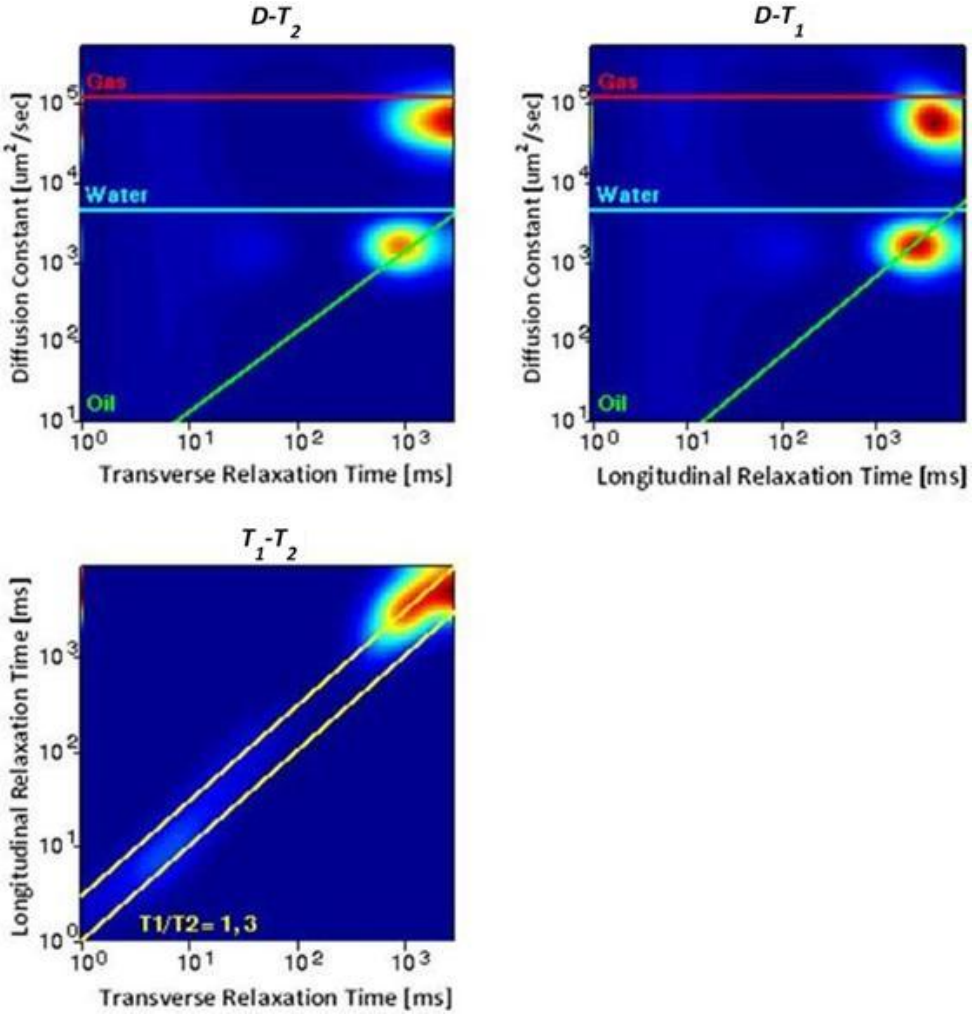

Figure 5.3: Field Case No. 1: *D*-T_1, *D*-T_2, and T_1-T_2 maps from NMR inversion results for the depth interval XX75-XX76 meters with a radial length of 2.7 inches from the borehole. From these maps, the same fluid types but more volume of virgin reservoir fluids and lesser volume of OBM can be detected.

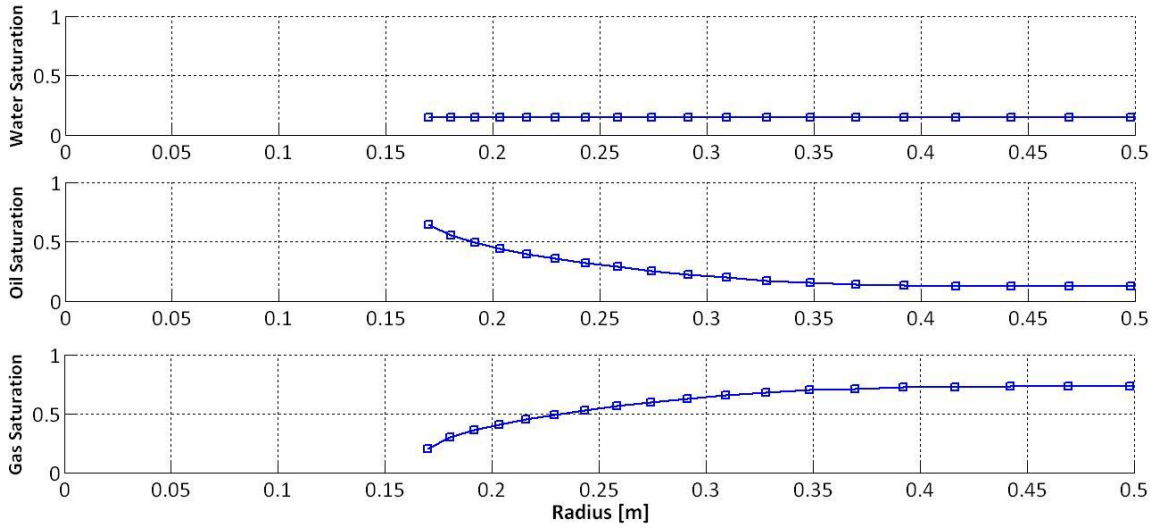

Figure 5.4: Numerically simulated radial profiles of water saturation, oil saturation, and gas saturation at the depths of XX75-XX76 meters. OBM filtrate invades into the formation from 0.16 meters, which is the radius of the borehole. While water saturation remains 0.15, oil saturation gradually decreases and gas saturation gradually increases as radial length increases.

Variable	**1.5 inches from the borehole**	**2.7 inches from the borehole**	**Units**
Saturation of bound water, S_{bw}	0.15	0.15	[ ]
Saturation of free water, S_{fw}	0.00	0.00	[ ]
Saturation of oil, S_{oil}	0.23	0.27	[ ]
Saturation of gas, S_{gas}	0.35	0.55	[ ]
Saturation of OBM, S_{OBM}	0.27	0.03	[ ]

Table 5.1: Summary of fluid saturations yielded from the radial fluid saturation profile for Field Case No. 1.

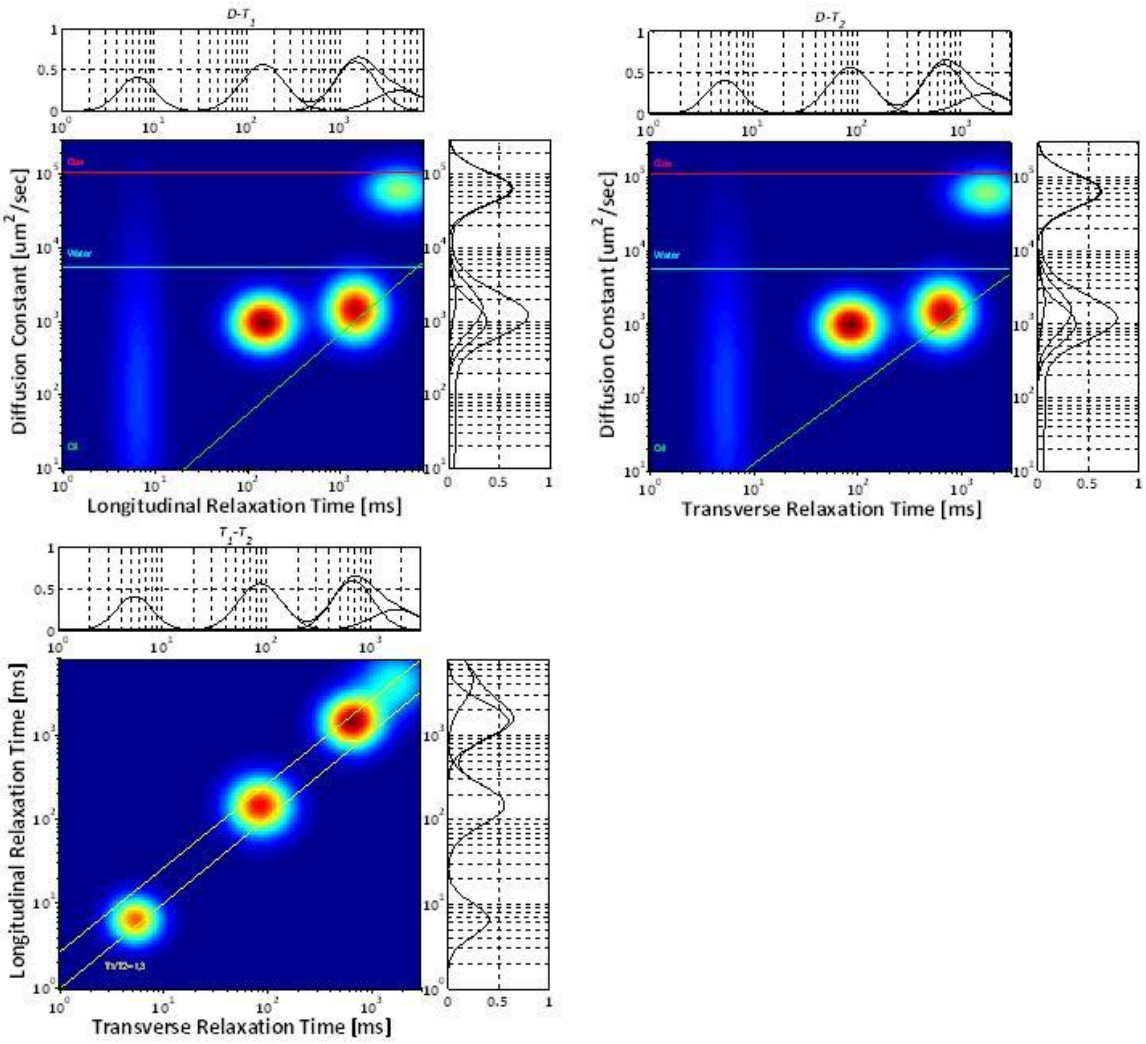

Figure 5.5: Field Case No. 1: *D*-T_1, *D*-T_2, and T_1-T_2 maps from 2D NMR simulations for the depth interval XX75-XX76 meters with a radial length of 1.5 inches from the borehole. From these maps, four explicit fluid signatures can be identified. These are gas, light oil, OBM, and a mixture of bound water and mud solid invasion.

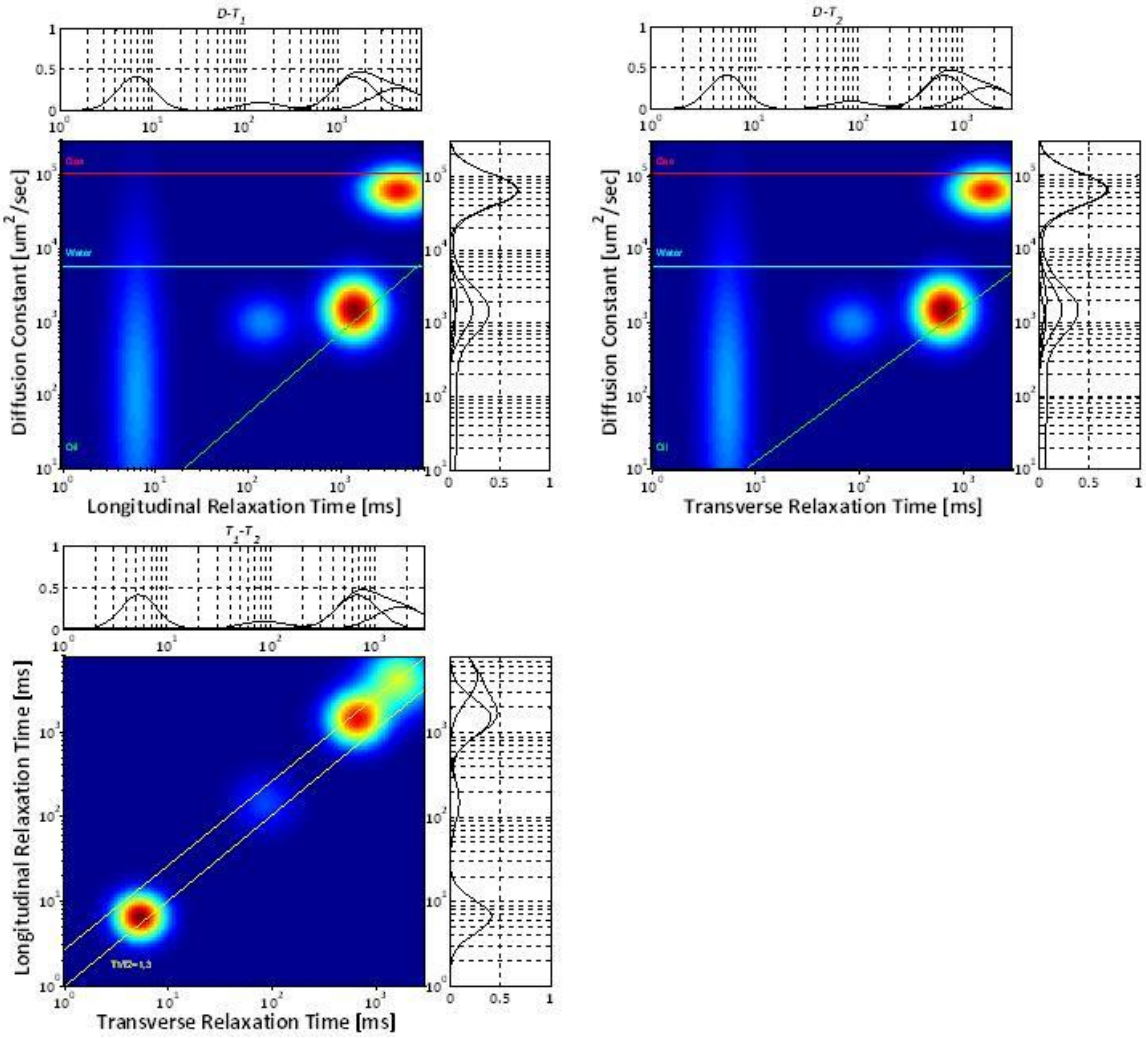

Figure 5.6: Field Case No. 1: *D*-T_1, *D*-T_2, and T_1-T_2 maps from 2D NMR simulations for the depth interval XX75-XX76 meters with a radial length of 2.7 inches from the borehole. From these maps, the same fluid types but more volume of virgin reservoir fluids and lesser volume of OBM can be detected.

5.2 FIELD CASE NO. 2: GAS-BEARING SILICICLASTIC FORMATION

The second field example shown in **Figure 5.7** describes the same well β, but at a lower depth interval of XX02-XX04 meters. Low Gamma-Ray log values indicate low shale concentration. High values of apparent resistivity logs and cross-over between bulk density and nuclear porosity confirm the presence of gas. Total porosity estimated with both NMR porosity and density porosity is approximately 30%. ECS mineralogy data indicates that this depth interval includes 3% pyrite. Because of its large magnetic susceptibility, internal magnetic field gradients can be affected. The T_2 cutoff for NMR distributions is 33 milliseconds.

Figures 5.8 and **5.9** show NMR inversion results from 1.5 inches and 2.7 inches from the borehole, respectively. These maps show fluid signatures for this interval depth are rich gas, OBM, bound water, and light oil. Rich gas signatures range in the area of high relaxation times and high diffusion constants. Signatures ranging in the area of low relaxation times are a mixture of OBM and bound water signatures of 6% exist for in-situ oil. A distinct difference between the two depths of investigation is the volume of OBM and rich gas. Although there are small amounts of movable water in this interval, OBM is mainly displacing gas, the dominating fluid. Again, due to the physics of mud-filtrate invasion, OBM signatures shown in **Figure 5.9** are smaller than those shown in **Figure 5.8**. Both NMR responses are masked by mud-filtrate, but stronger OBM signatures are evident at shallower radial distance. Smaller volumes of OBM and more in-situ fluids, in this case, mainly gas, were found in **Figure 5.9** due to the longer radial distance.

The algorithm discussed in Chapter 3 also reproduces the NMR inversion results described above. Petrophysical parameters from static and dynamic simulations and fluid saturations from **Figure 5.10** were input into the algorithm. **Table 5.2** reports fluid

saturations at a distance of 1.5 inches and 2.7 inches from the wellbore. **Figures 5.11** and **5.12** are NMR D-T_1, D-T_2, and T_1-T_2 simulation results at corresponding depths of investigation, respectively.

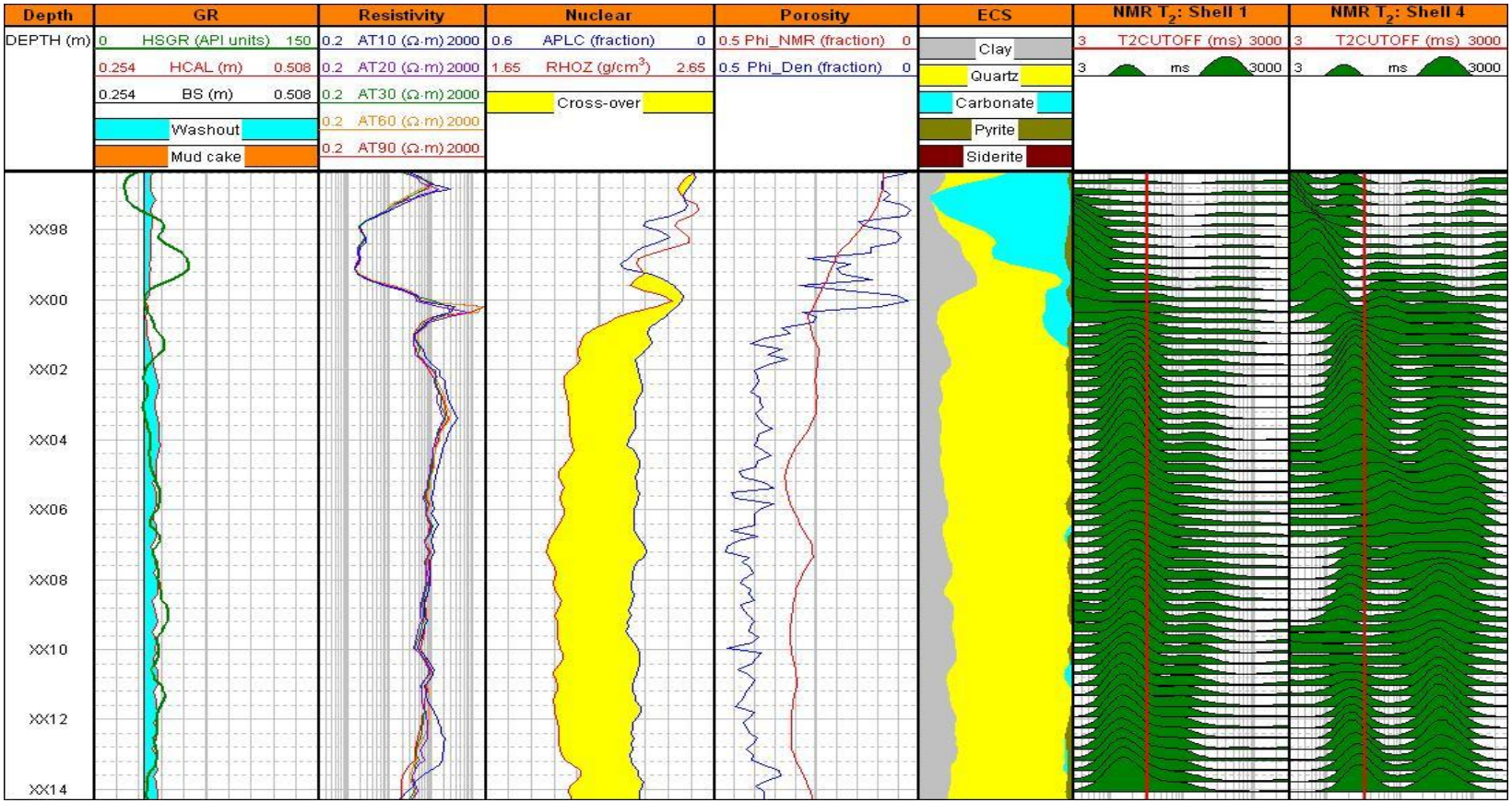

Figure 5.7: Field Case No. 2: Wireline logs along the depth interval of interest. Track 1: depth. Track 2: Gamma-Ray log, bit size, caliper log, washouts, and mud cake thickness. Track 3: apparent resistivity logs. Track 4: bulk density and neutron porosity calibrated in sandstone porosity units and their corssover. Track 5: NMR porosity and density porosity. Track 6: ECS mineralogy data with clay, quartz, carbonate, pyrite, and siderite. Track 7: T_2 distributions measured at 1.5 inches from the borehole. Track 8: T_2 distributions measured at 2.7 inches from the borehole.

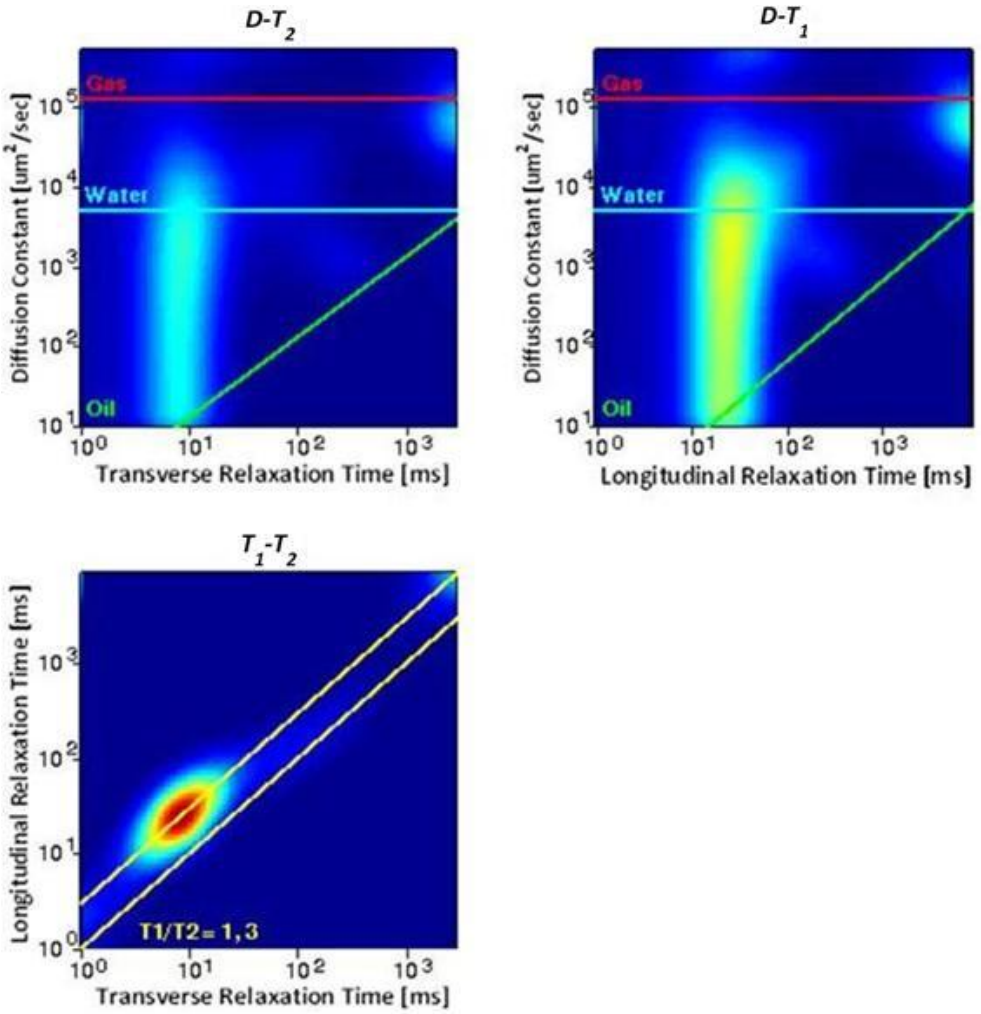

Figure 5.8: Field Case No. 2: D-T_1, D-T_2, and T_1-T_2 maps from NMR inversion results for the depth interval XX02-XX04 meters with a radial length of 1.5 inches from the borehole. The strong fluid signatures with high T_1/T_2 ratio are a mixture of bound water and OBM. Gas and in-situ oil is exhibited by relatively weak signatures.

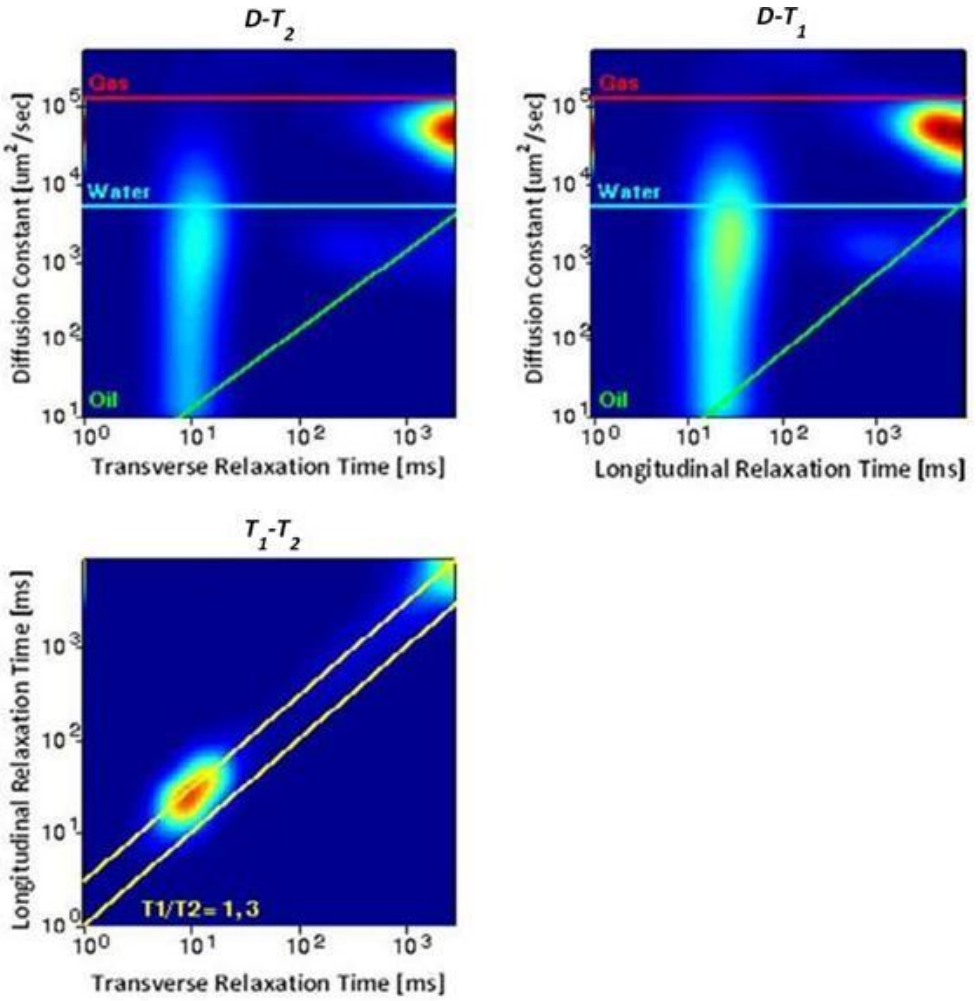

Figure 5.9: Field Case No. 2: D-T_1, D-T_2, and T_1-T_2 maps from NMR inversion results for the depth interval XX02-XX04 meters with a radial length of 2.7 inches from the borehole. From these maps, the same fluid types but more volume of virgin reservoir fluids and lesser volume of OBM can be diagnosed.

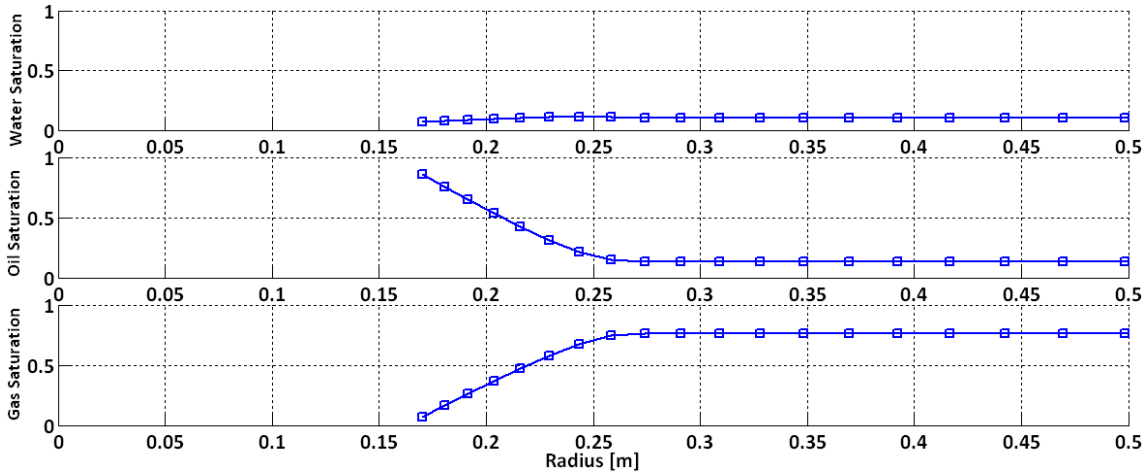

Figure 5.10: Numerically simulated radial profiles of water saturation, oil saturation, and gas saturation at the depths of XX02-XX04 meters. OBM saturation gradually decreases, whereas gas and water saturations gradually increase as radial length increases.

Variable	**1.5 inches from the borehole**	**2.7 inches from the borehole**	**Units**
Saturation of bound water, S_{bw}	0.07	0.07	[ ]
Saturation of free water, S_{fw}	0.00	0.03	[ ]
Saturation of oil, S_{oil}	0.06	0.06	[ ]
Saturation of gas, S_{gas}	0.33	0.58	[ ]
Saturation of OBM, S_{OBM}	0.54	0.26	[ ]

Table 5.2: Summary of the fluid saturations yielded from the radial fluid saturation profile for Field Case No. 2.

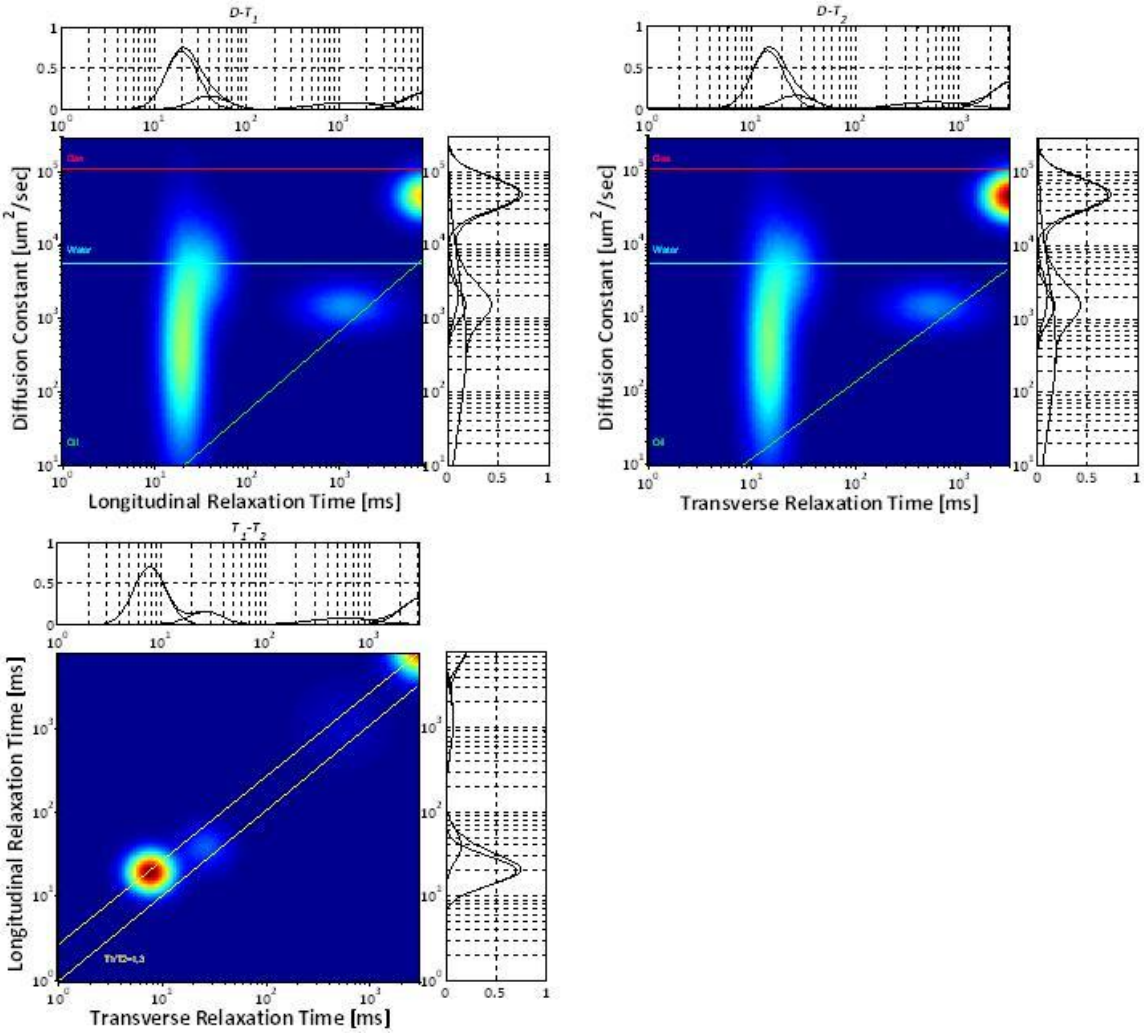

Figure 5.11: Field Case No. 2: D-T_1, D-T_2, and T_1-T_2 maps from 2D NMR simulations for the depth interval XX02-XX04 meters with a radial length of 1.5 inches from the borehole. The strong fluid signatures with high T_1/T_2 ratio are a mixture of bound water and OBM. Gas and in-situ oil are indicated by relatively weak signatures.

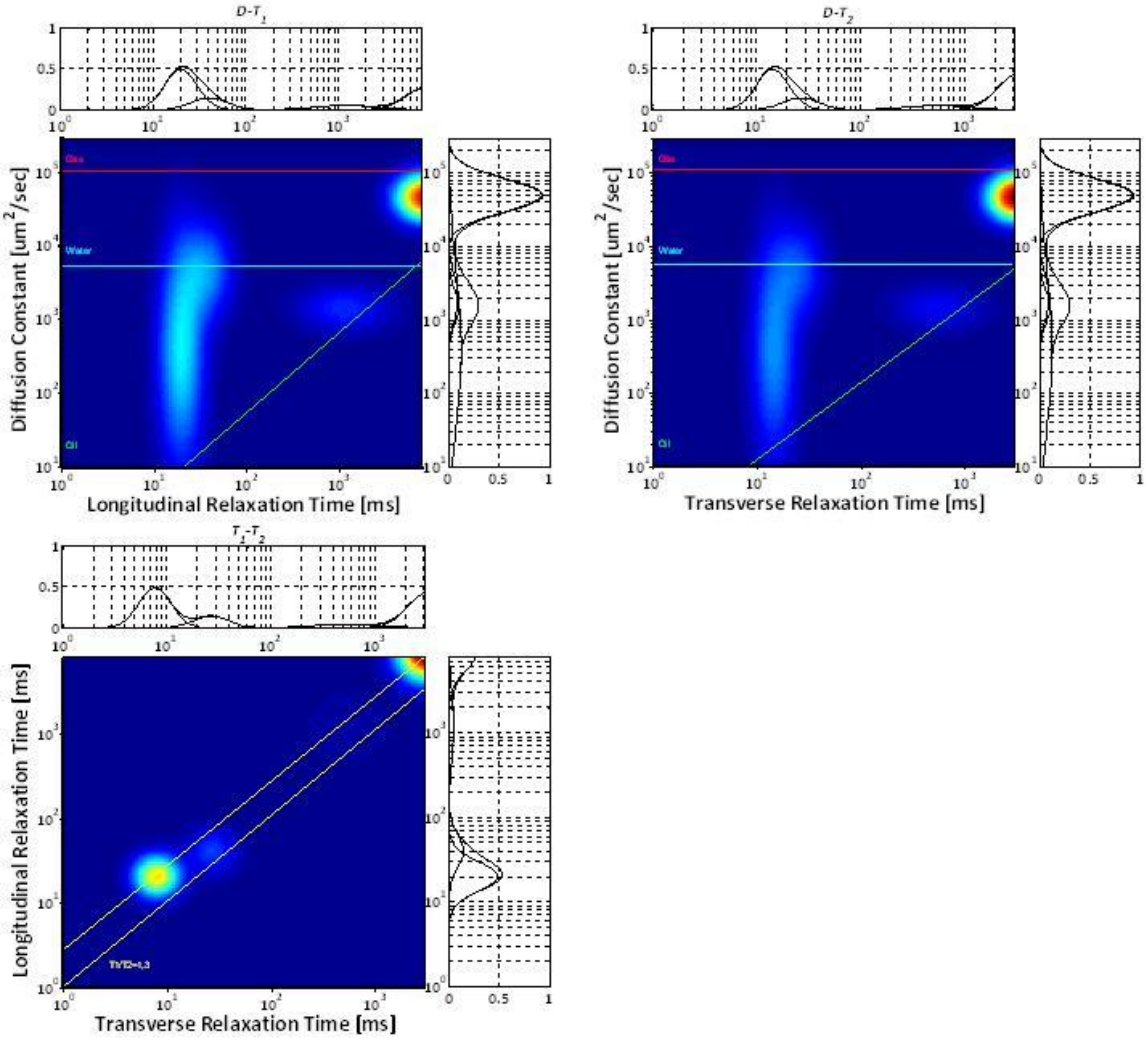

Figure 5.12: Field Case No. 2: *D*-T_1, *D*-T_2, and T_1-T_2 maps from 2D NMR simulations for the depth interval XX02-XX04 meters with a radial length of 2.7 inches from the borehole. From these maps, the same fluid types but more volume of virgin reservoir fluids and lesser volume of OBM can be predicted.

Chapter 6: Multi-dimensional NMR inversions

This chapter describes the theory of forward modeling and inversions for 2D NMR data. Various kinds of 2D NMR maps, including D-T_2 and T_1-T_2 maps can be acquired from echo decay sequences and vice versa. The inversion examples of field data with two different depths of investigation will be discussed.

6.1 THEORY

Figure 6.1 illustrates the NMR forward and inverse process graphically. Inversion is to fit the echo decay sequence in the time domain to the T_2 distributions. Conversely, transforming T_2 distributions to the echo decay sequence is called forward modeling.

For the 2D forward and inverse technique, one needs several different echo decay sequences with different polarization times, *TW*, and different inter-echo time, *TE*, to contrast fluid diffusivities. The saturation profiling sequence parameters used in the inversions are tabulated in **Table 6.1**. Whereas measurement 1 with a long *TW* value is designed to polarize all the hydrogen protons in the reservoir, measurements 11 and 12 are designed to polarize the bound water only. These saturation profiling sequence parameters have been previously studied (Minh et al., 2003, Toumelin and Sun, 2009). **Figure 6.2** shows the example of 2D forward modeling and inversion graphically.

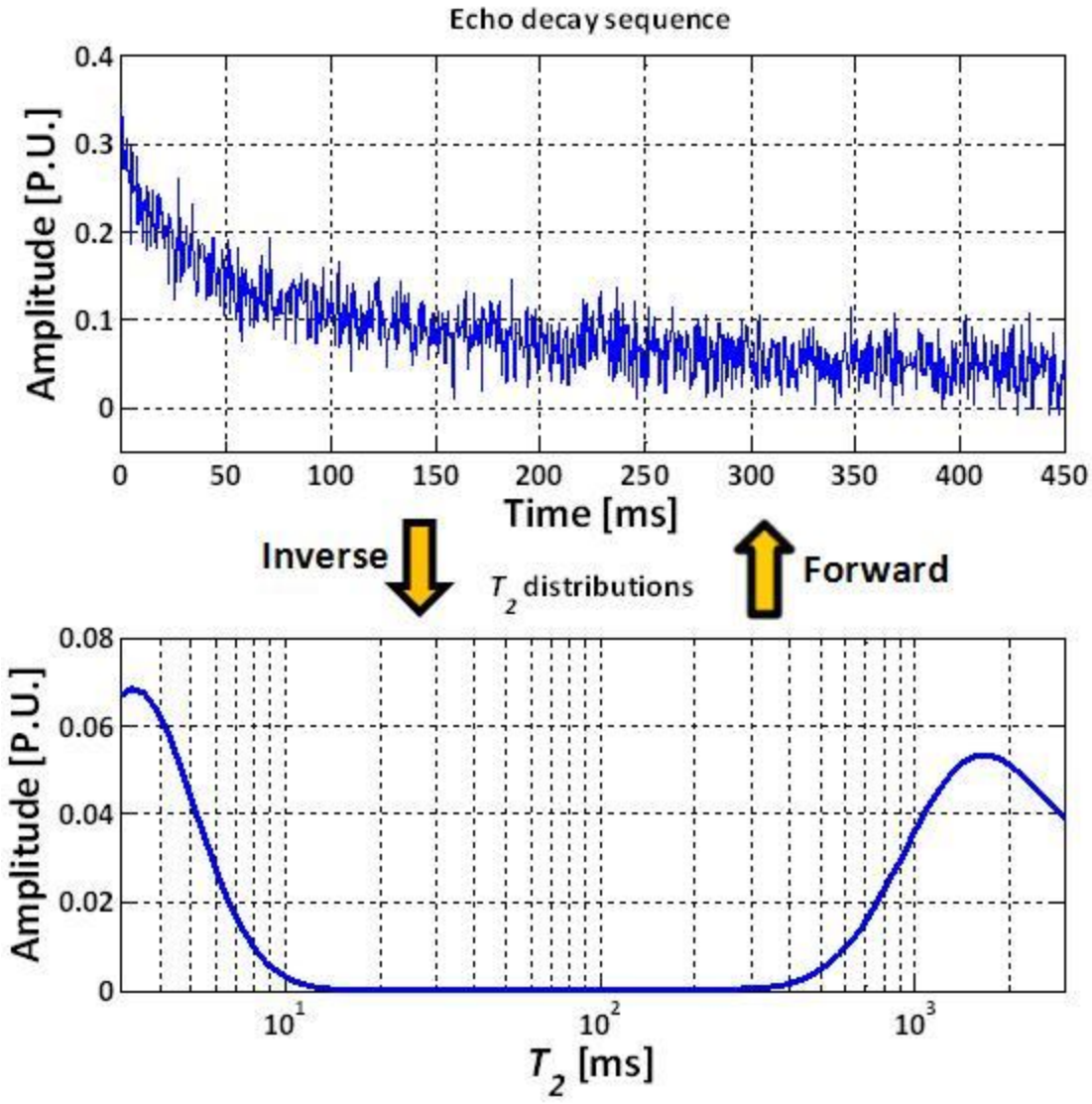

Figure 6.1: Graphical descriptions of forward and inverse modeling. These plots show how an echo decay sequence in time domain is converted into a T_2 distribution and vice versa. Note that the first value of the echo decay sequence and the area under the T_2 distribution curve are the same as total porosity.

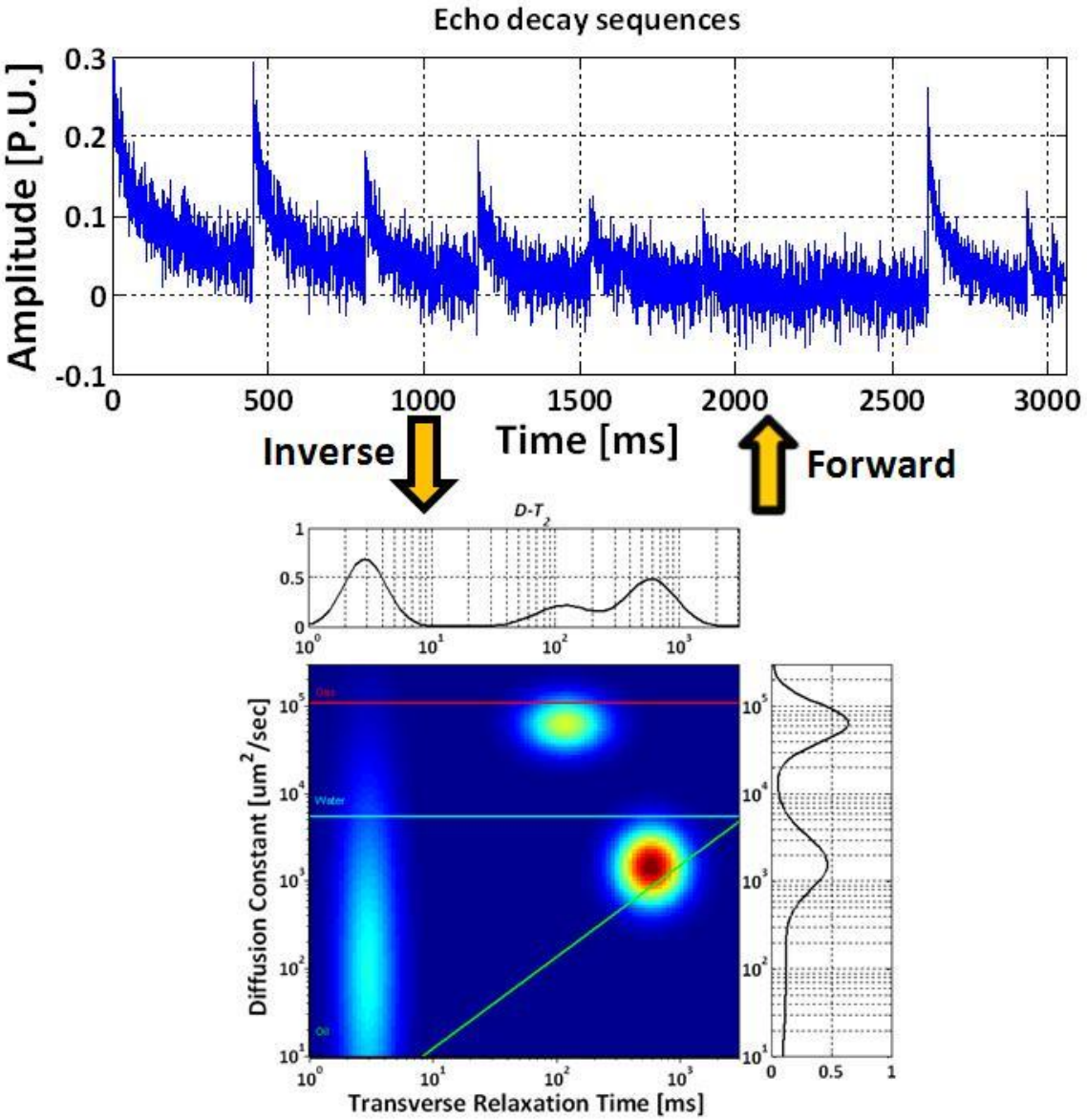

Figure 6.2: Graphical descriptions for 2D forward and inverse modeling. These plots show how echo decay sequences in the time domain are converted into a *D*-T_2 map and vice versa. Note that each decay sequence has a different value of inter-echo time and polarization time. Whereas polarization time governs the polarization, inter-echo time determines the decay of fluid magnetizations.

Measurements [ ]	***TW*** **[ms]**	***TE*** **[ms]**	***TEL*** **[ms]**	**REPS** [ ]	**NECHOES** [ ]
1	9,800	0.45	0.45	1	1002
2	2,400	0.45	0.45	1	802
3	1,200	0.45	2.00	1	802
4	1,200	0.45	3.00	1	802
5	1,200	0.45	5.00	1	802
6	1,200	0.45	8.00	1	802
7	1,200	0.45	12.00	2	802
8	800	0.45	0.45	2	700
9	100	0.45	0.45	2	192
10	32	0.45	0.45	2	64
11	8	0.45	0.45	32	16
12	9,700	0.60	0.60	1	752
13	2,500	0.60	0.60	1	602
14	1,200	0.60	5.00	1	602
15	1,200	0.60	4.00	1	602
16	1,200	0.60	7.00	1	602
17	1,200	0.60	10.00	1	602
18	1,200	0.60	16.00	1	602
19	800	0.60	0.60	1	512
20	100	0.60	0.60	1	144
21	32	0.60	0.60	1	64
22	8	0.60	0.60	32	16

Table 6.1: Profiling sequence parameters used in forward modeling and inversion. Measurements 1 to 11 and measurements 12 to 22 are designed to detect hydrogen protons from the radial depth of 1.5 inches and 2.7 inches from the borehole, respectively. Whereas the *TW* controls the polarization of the hydrogen protons, the inter-echo time, *TE* controls the decay of the magnetization. Various combinations of *TW* and *TE* are necessary to diagnose all fluid types shown on 2D NMR maps.

The NMR echo decay sequence inversion is widely used by the oil industry. The inversion from NMR measurements to attain the T_2 distributions has the following form

$$M_{o,p,q}(t,TW,TE,G)=\sum_{k=1}^{m}\sum_{i=1}^{n}\sum_{j=1}^{l}a_{i,j,k}(1-\mathrm{e}^{-\frac{TW_q}{T_{1,k}}})\mathrm{e}^{-\frac{t_o}{T_{2,i}}}\mathrm{e}^{-\frac{D_j(TE_p*G*\gamma)^2t}{12}}+\varepsilon_{o,p,q}, \tag{6.1}$$

where $M_{o,p,q}$ is the amplitude of the magnetization decay sequence using TE_p and TW_q with a noise of $\varepsilon_{o,p,q}$ at a time t_o, and $a_{i,j,k}$ is proton density distribution function (the amplitude of T_2) to be solved (Jerath, 2011). Each $T_{1,k}$, $T_{2,i}$, and D_j has sampling numbers of m, n, and l equally spaced on a logarithmic scale, respectively. One can separate the kernel represented in equation (6.1) into three kernels, which can be written as

$$k_1(T_1,TW)=(1-e^{-\frac{TW}{T_1}}), \tag{6.2}$$

$$k_2(t,T_2)=\mathrm{e}^{-\frac{t}{T_2}}, \tag{6.3}$$

and

$$k_3(t,TE,D)=\mathrm{e}^{-\frac{D(TE*G*\gamma)^2t}{12}}, \tag{6.4}$$

where k_1 is the T_1 kernel, k_2 is the T_2 kernel, and k_3 is the diffusion kernel (Sun and Dunn, 2005). Equation (6.1) can be expressed as a Fredholm integral equation of the first kind (IFKs) (Aster el al., 2005):

$$M(t,TW,TE)=\int\int\int a(T_1,T_2,D)k_1(T_1,TW)k_2(t,T_2)k_3(t,TE,D)dDdT_1dT_2+\varepsilon. \tag{6.5}$$

With a sufficiently long TW, the T_1 kernel increases to 1 and equation (6.5) simplifies to

$$M(t,TE) = \int\int a(T_2, D) k_2(t, T_2) k_3(t, TE, D) dD dT_2 + \varepsilon . \quad (6.6)$$

The coupled T_2 kernel and diffusion kernel can be implemented into the NMR 2D inversion to obtain the D-T_2 map. In the same manner, one can derive the T_1-T_2 map using coupled T_1 kernel and T_2 kernel by removing diffusion kernel as follows:

$$M(t,TW) = \int\int a(T_1, T_2) k_1(T_1, TW) k_2(t, T_2) dT_1 dT_2 + \varepsilon . \quad (6.7)$$

To solve equations (6.6) and (6.7), the data should be compressed before implementing inversions. Modern NMR logging tools provide several echo decay sequences that have hundreds sampling points each, the data points used in matrix calculations are too numerous for efficient inversion. To reduce computational time, each decay sequence is compressed individually to have manageable sampling points. The singular value decomposition (SVD) method using the kernels described in equations (6.6) and (6.7) provides a diagonal matrix and a unitary matrix (Dunn, Bergman, and Latorraca, 2002). With these matrices and the compressed data, one can find an optimized regularization parameter, α, using the L-curve method (Hansen, 2007).

Equation (6.6) or (6.7) can be expressed in vector form,

$$M = k \bullet a , \quad (6.8)$$

where k is the combination of corresponding kernels and a is the proton density distribution function. The solution of the least-squares minimization for equation (6.8) can be expressed as

$$k^T \bullet M = k^T \bullet k \bullet a , \quad (6.9)$$

$$a = (k^T \bullet k)^{-1} \bullet k^T \bullet M \,. \tag{6.10}$$

The exponential property of the kernel k causes the estimation of the proton density distribution function to be an ill-posed problem. To approach this problem, mathematicians have developed diverse techniques.. One of the most popular methods is to add a penalty function into the cost function to smooth the solution. Implementing the well-known Tikhonov regularization method (Tikhonov and Arsenin, 1997) with optimized regularization parameter, α, equation (6.10) can be written as

$$a = (k^T \bullet k + \alpha^2 I)^{-1} \bullet k^T \bullet M \,. \tag{6.11}$$

After applying the model weighting matrix, W_x and the data weighting matrix, W_d into equation (6.11), the final cost function that needs to be minimized becomes

$$C(a) = \left\| W_d \bullet (k \bullet a - M) \right\|_2^2 + \alpha^2 \left\| W_x \bullet a \right\|_2^2 . \tag{6.12}$$

For this linear inversion, a non-negative constraint is usually applied to prevent the proton density distribution function from having negative values.

6.2 METHOD

The forward modeling starts with the 2D NMR data simulated in Chapter 5. The 2D proton density distribution function, which originally has a size of n by n, can be rearranged to a column vector of n^2 by 1. To reconstruct echo decay sequences, the

discretized kernel should be multiplied to the proton density distribution function, as described in equation (6.8).

$$\begin{bmatrix} M_1 \\ M_2 \\ M_3 \\ \vdots \\ M_m \end{bmatrix} = \begin{bmatrix} k_{11} & k_{12} & \cdots & k_{1n^2} \\ k_{22} & \ddots & \ddots & k_{2n^2} \\ k_{23} & \ddots & \ddots & k_{3n^2} \\ \vdots & \ddots & \ddots & \vdots \\ k_{mn^2} & \cdots & \cdots & k_{mn^2} \end{bmatrix} \bullet \begin{bmatrix} a_1 \\ a_2 \\ a_3 \\ \vdots \\ a_{n^2} \end{bmatrix}. \tag{6.13}$$

Figure 6.3 compares the reconstructed echo decay sequences and the measurements. One of the benefits of NMR inversion with the reconstructed echo decay sequences instead of the measured echo decay sequences is that the reconstructed echo decay sequences have no noise while the measurements have high signal to noise ratio (SNR). After having the reconstructed echo decay sequences, inversion provides the 2D proton density distribution function can be expressed as the augmented matrix form;

$$\begin{bmatrix} a_1 \\ a_2 \\ \vdots \\ \vdots \\ \vdots \\ \vdots \\ a_{n^2} \end{bmatrix} = \begin{bmatrix} k_{11} & k_{12} & \cdots & k_{1n^2} \\ k_{22} & \ddots & \ddots & k_{2n^2} \\ \vdots & \ddots & \ddots & \vdots \\ k_{mn^2} & \cdots & \cdots & k_{mn^2} \\ W_{x11} & W_{x12} & \cdots & W_{x1n^2} \\ W_{x21} & \ddots & \ddots & W_{x2n^2} \\ \vdots & \ddots & \ddots & \vdots \\ W_{xn^2 1} & \cdots & \cdots & W_{xn^2 n^2} \end{bmatrix} \backslash \begin{bmatrix} M_1 \\ M_2 \\ \vdots \\ M_m \\ 0 \\ 0 \\ \vdots \\ 0 \end{bmatrix} \tag{6.14}$$

This is the linear least-squares minimization problem.

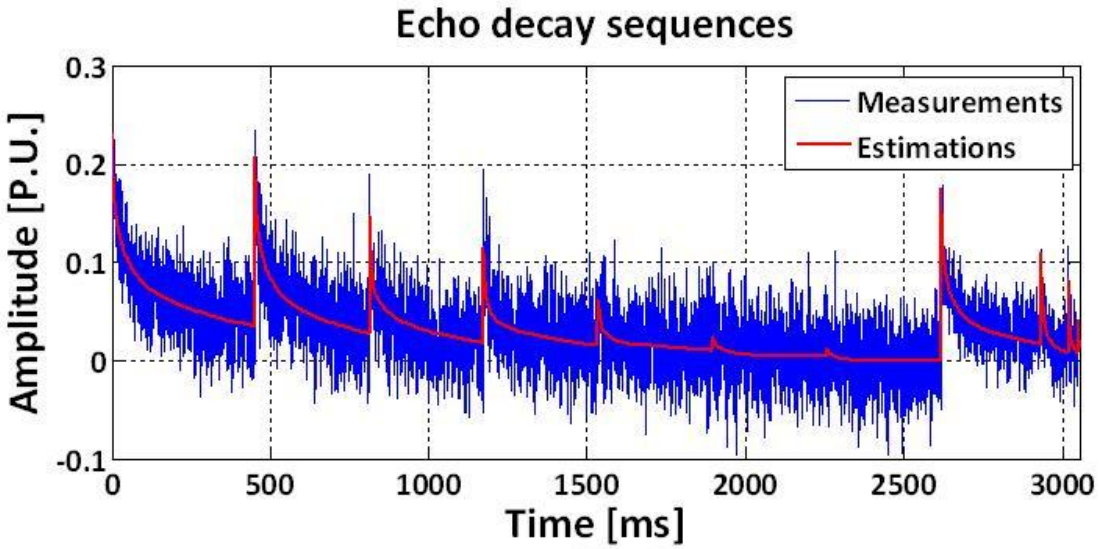

Figure 6.3: Comparison of reconstructed echo decay sequences with measured echo decay sequences. The echo decay sequences in blue are the measurements; those in red are the estimations.

6.3 INVERSION RESULTS

These 2D NMR forward modeling and inversion algorithms were applied to Field Cases No.1 and 2 analyzed in Chapter 5. **Figure 6.4**, panels (a) and (b) show the simulated 2D NMR maps, and panels (c) and (d) show the corresponding 2D NMR maps of inversion results. Detail observation of both D-T_2 and T_1-T_2 maps reveals a small discrepancy between simulation results and inversion results, but overall they are in acceptable agreement. **Figure 6.5** shows the 2D NMR maps at the same depth of interval and a longer radial depth of investigation of 2.7 inches. Again, inversion results on panel (c) and (d) have proton density distributions similar to those from the 2D NMR simulations. D-T_2 maps are more reliable than T_1-T_2 maps for a variety of applications,

including fluid typing (Toumelin et al., 2004). The major difference between **Figures 6.4** and **6.5** is OBM signatures ranging within relaxation times of 100 milliseconds.

The simulated 2D NMR maps for the second field case are shown in **Figure 6.6,** panels (a) and (b). Dominant fluids in these maps are bound water and OBM. These signatures also can be observed on panels (c) and (d), which describe the inversion results. However, inversion tends to stretch out the signal over a broad range of the diffusion constant. This is a practical limitation of diffusion measurements: for fluids with T_2 values of less than about 20 milliseconds, it is impossible to determine the corresponding diffusion rate (Freedman et al., 2003; Heaton et al., 2004). **Figure 6.7** shows the same D-T_2 and T_1-T_2 maps for the same depth of interval with a longer radial depth of investigation.

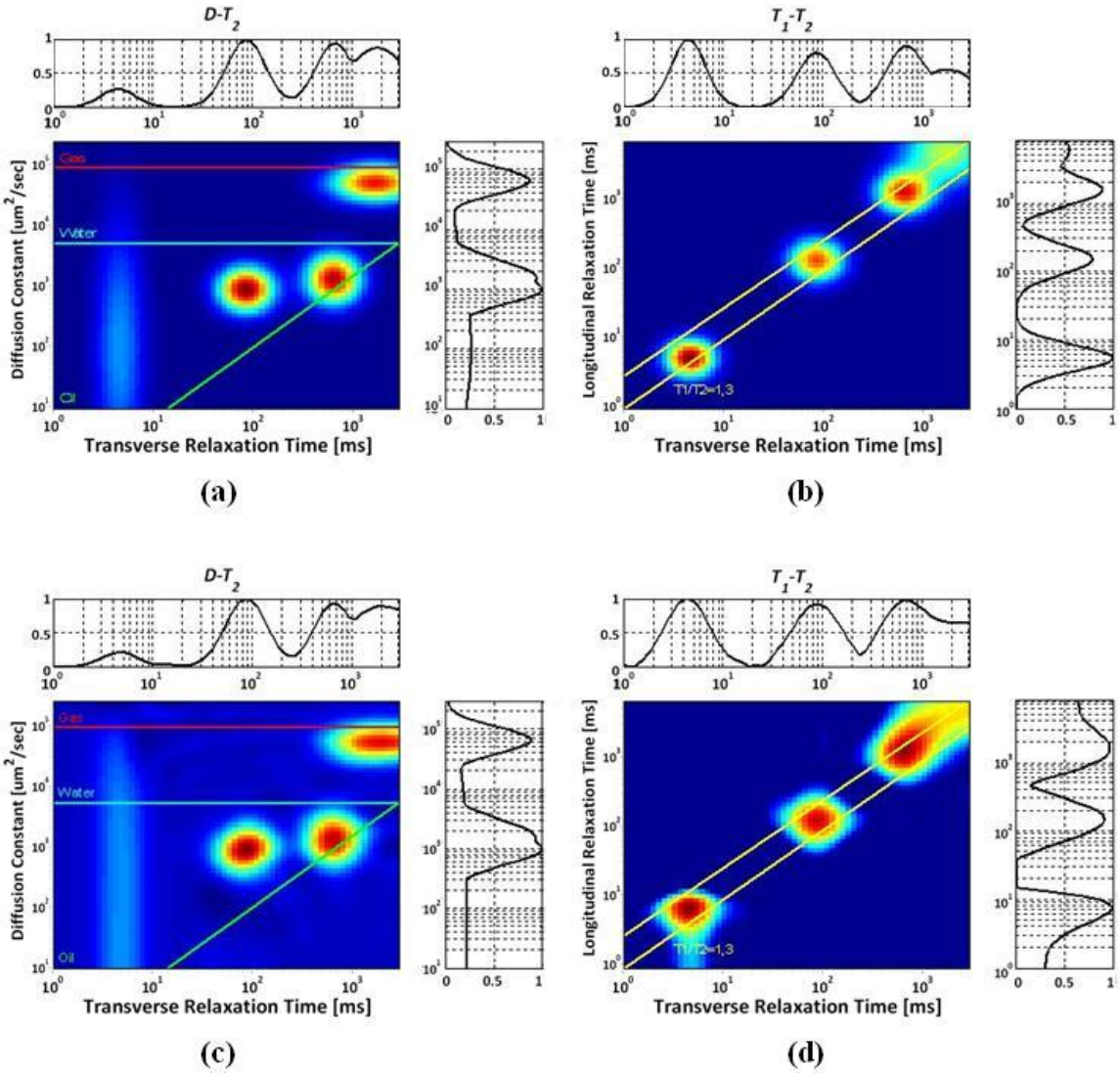

Figure 6.4: *D*-T_2 and T_1-T_2 maps from 2D NMR simulation and those from the inversion for the depth interval XX75-XX76 meters with a radial length of 1.5 inches from the borehole. Panels (a) and (b) show the 2D NMR simulation results used for the forward modeling to reconstruct echo decay sequences. Panels (c) and (d) show the 2D proton density distribution function generated by inversion using these reconstructed echo decay sequences.

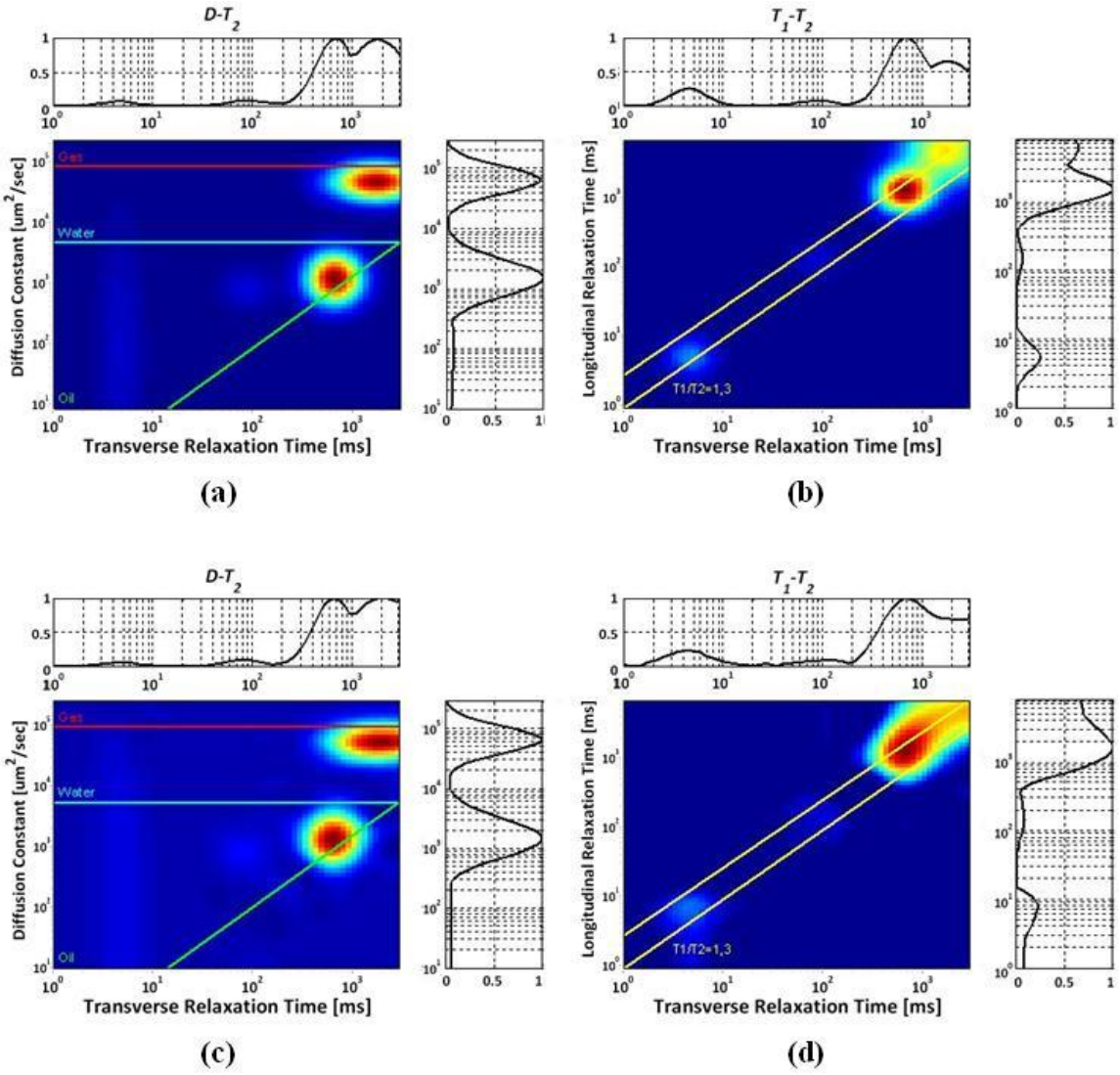

Figure 6.5: *D*-T_2 and T_1-T_2 maps from 2D NMR simulation and those from the inversion for the depth interval XX75-XX76 meters with a radial length of 2.7 inches from the borehole. Panels (a) and (b) show the 2D NMR simulation results used for the forward modeling to reconstruct echo decay sequences. Panels (c) and (d) show the 2D proton density distribution function generated by inversion using these reconstructed echo decay sequences.

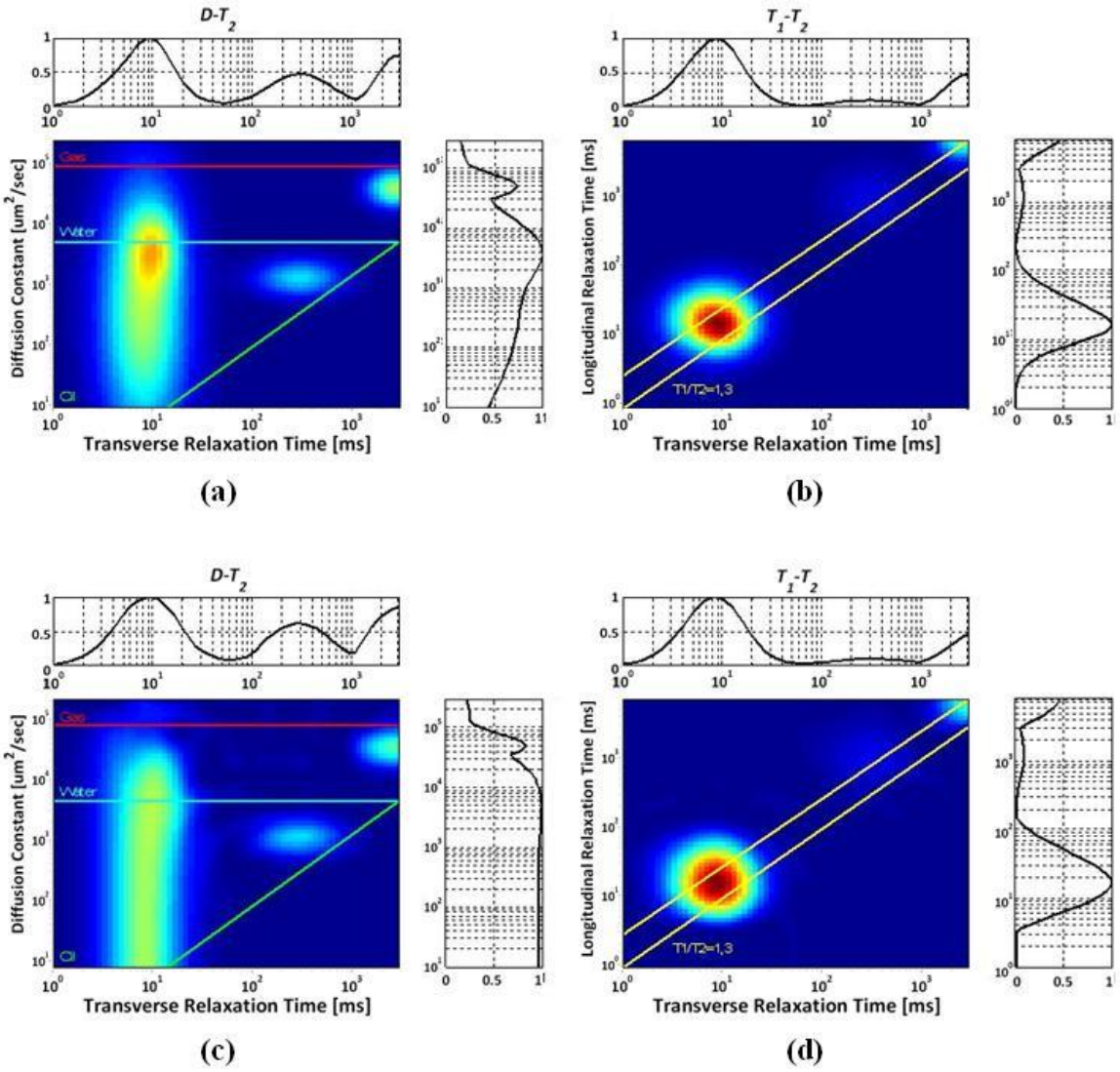

Figure 6.6: D-T_2 and T_1-T_2 maps from 2D NMR simulation and those from the inversion for the depth interval XX02-XX04 meters with a radial length of 1.5 inches from the borehole. Panels (a) and (b) show the 2D NMR simulation results used for the forward modeling to reconstruct echo decay sequences. Panels (c) and (d) show the 2D proton density distribution function generated by inversion using these reconstructed echo decay sequences.

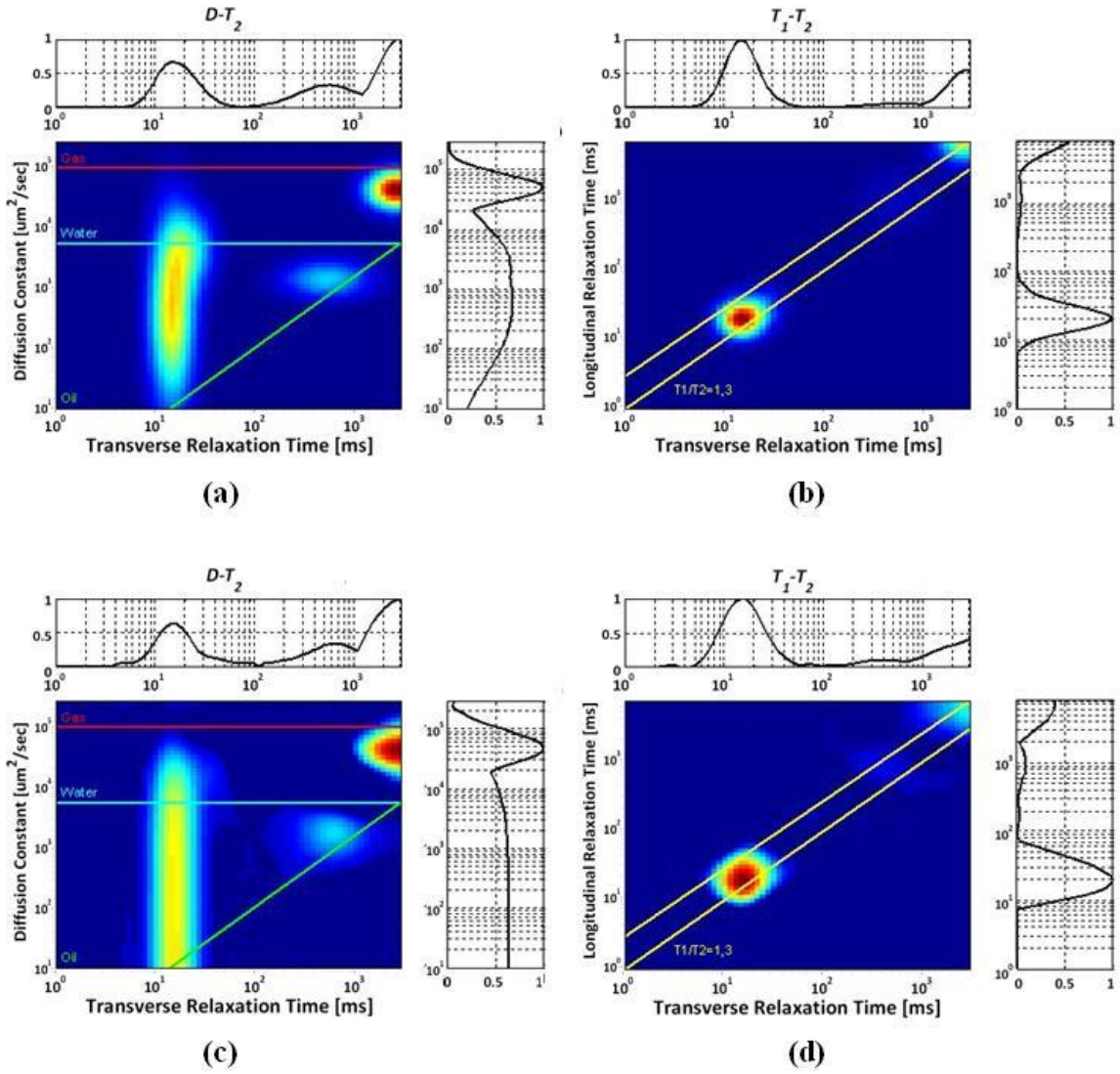

Figure 6.7: D-T_2 and T_1-T_2 maps from 2D NMR simulation and those from the inversion for the depth interval XX02-XX04 meters with a radial length of 2.7 inches from the borehole. Panels (a) and (b) show the 2D NMR simulation results used for the forward modeling to reconstruct echo decay sequences. Panels (c) and (d) show the 2D proton density distribution function generated by inversion using these reconstructed echo decay sequences.

Chapter 7: Conclusions and Recommendations

This chapter presents the recommended best practices to simulate the process of mud-filtrate invasion. It also reports multi-dimensional NMR simulations to cross-validate the physics of mud-filtrate invasion. The summary emphasizes the significance of integrated interpretation of NMR measurements with mud-filtrate invasion. Additionally, it discusses the conclusions stemming from NMR inversion results and mentions the limitations of the method.

7.1 Recommended Best Practices

The workflow introduced in this thesis summarizes recommended best practices for invasion-consistent interpretation of NMR measurements. Prior to interpreting NMR measurements, building static and dynamic simulations with conventional logs is suggested, in order to acquire petrophysically consistent models. Static simulations include a GR log, a density log, a neutron log, and five resistivity logs to estimate common petrophysical properties such as porosity, volumetric shale concentration, initial water saturation, and mineral compositions.

After static reservoir models with associated petrophysical properties are built, simulation of mud-filtrate invasion is employed to determine dynamic petrophysical properties, including wetting and non-wetting phase saturations, capillary pressure, absolute permeability, and relative permeability. In order to have good matches between reconstructed well logs and available well logs, several iterative readjustments for static and dynamic properties are needed.

Based on the petrophysical parameters obtained from both static and dynamic models, radial fluid saturation profiles for water, oil, and gas can be estimated. The 2D

NMR simulations with the petrophysical parameters and saturation values from radial fluid saturation profiles provide various 2D maps, including D-T_2 and T_1-T_2 maps. Agreements between 2D NMR maps from simulations and those from inversions yield reliable interpretation of NMR measurements.

7.2 CONCLUSIONS

This section lists the most important conclusions stemming from this thesis.

i. Construction of static and dynamic models using UTAPWeLS honors physics of mud-filtrate invasion and available well logs including Gamma-Ray, nuclear, and resistivities logs. Numerical simulations of mud-filtrate invasion yield a quantitative and reliable estimation of radial fluid distributions.

ii. NMR measurements exhibit a shallow depth of investigation. Mud-filtrate displaces in-situ reservoir fluids, their NMR response can be masked by this invading fluid. Measurements taken at the radial distance farther from the borehole, stronger in-situ fluid signatures are observed in the radial fluid saturation profile. This is because mud-filtrate saturation gradually decreases as the radial length increases. The 2D NMR simulations at multiple depths of

investigation consistently cross-validate near borehole fluid distributions due to mud-filtrate invasion.

iii. Conventional NMR T_2 distribution cannot differentiate gas signatures from water signatures in most cases. Multi-dimensional NMR interpretation techniques have advantages over conventional NMR interpretations for fluid typing because they reveal contrasts in fluid diffusion coefficient.

iv. NMR responses to neutral to oil-wet formations differ from those of water-wet formations. As more oil bubbles come in contact with grains, the surface relaxation times of oil increase and the corresponding relaxation times decrease. Consequently, decreased surface relaxation of the water lengthens relaxation times.

v. NMR responses for kerogen contained in nano-scaled pores are quite different from those in conventional reservoirs. In general, dominant surface relaxation causes both water and gas signatures to move T_2 ranges within a few milliseconds because of extremely small pore sizes. Also, gas signatures have decreased diffusion coefficients due to adsorbed gas.

vi. Inversion results of the NMR 2D maps of D-T_2 and T_1-T_2 are in good agreement with both NMR simulation results. Since NMR inversion results

are derived from several echo decay sequences that are independent of GR, density, neutron, and resistivity logs, agreements between NMR simulation results and inversion results at different DOIs provide invasion-consistent interpretations. The challenge of this inversion technique is to find exact diffusion constants for the fluids with T_2 values of less than about 20 milliseconds. The signature of these fluids tends to be elongated over an extended range of diffusion constants.

vii. Water, oil, and gas saturations from inversion using NMR measurements at two different DOIs are consistent with corresponding saturations simulated from the radial fluid saturation profiles given by UTAPWeLS for field case examples. Dynamic simulation plays a crucial role in quantifying how much in-situ fluid was displaced by mud-filtrate invasion for field case examples because it is difficult to separate formation oil from OBM filtrate completely.

7.3 RECOMMENDATIONS FOR FUTURE WORK

The NMR inversions to construct D-T_1 maps have not been taken into account in this thesis. Projection from the 3D proton density distribution function of D-T_1-T_2 onto the D-T_1 plane can provide D-T_1 maps because the diffusion kernel and the T_1 kernel are not coupled. Further investigations to calculate optimized profiling sequence parameters for the linear inversion would help to improve the accuracy of interpretations. Core data can be used to verify porosity and water saturation estimated from static and dynamic

simulations, and NMR inversions. Possible applications of reliable fluid identifications using NMR 2D maps include estimations of in-situ hydrocarbon properties. Empirical correlations using T_1, T_2, or diffusion coefficients can be utilized to predict oil viscosity and Gas to Oil Ratio (GOR). Understanding these parameters can in turn improve reservoir characterization and possibly increase oil and gas production.

Appendix: Wettability Tests

This appendix describes how to measure wettability of a fluid. Wettability is the ability of a fluid to maintain contact with a solid surface in the presence of other immiscible fluid. In a petroleum reservoir, either water or oil can be a wetting phase, whereas gas is always considered to be a non-wetting phase.

There are several methods to determine reservoir wettability, measured as a wettability index. The Amott wettability test (Amott, 1959) and the United States Bureau of Mines (USBM) wettability test (Donaldson et al., 1969) provide the standard wettability indexes of reservoir core samples.

A.1 Amott wettability test

Amott's wettability test (1959) is one of the most widely used methods for measuring the wettability of core samples. This method consists of four steps, two of which are spontaneous imbibition measurements and two are forced displacement measurements:

1. Prepare the core sample initially saturated with water. Measure the volume of water displaced by the spontaneous imbibition of oil for 20 hours.
2. Measure the additional volume of water displaced by the centrifugal displacement.
3. After forced displacement measurement, immerse the core in water and measure the volume of oil displaced by the spontaneous imbibition of water for 20 hours.
4. Measure the additional volume of oil displaced by the centrifugal displacement.

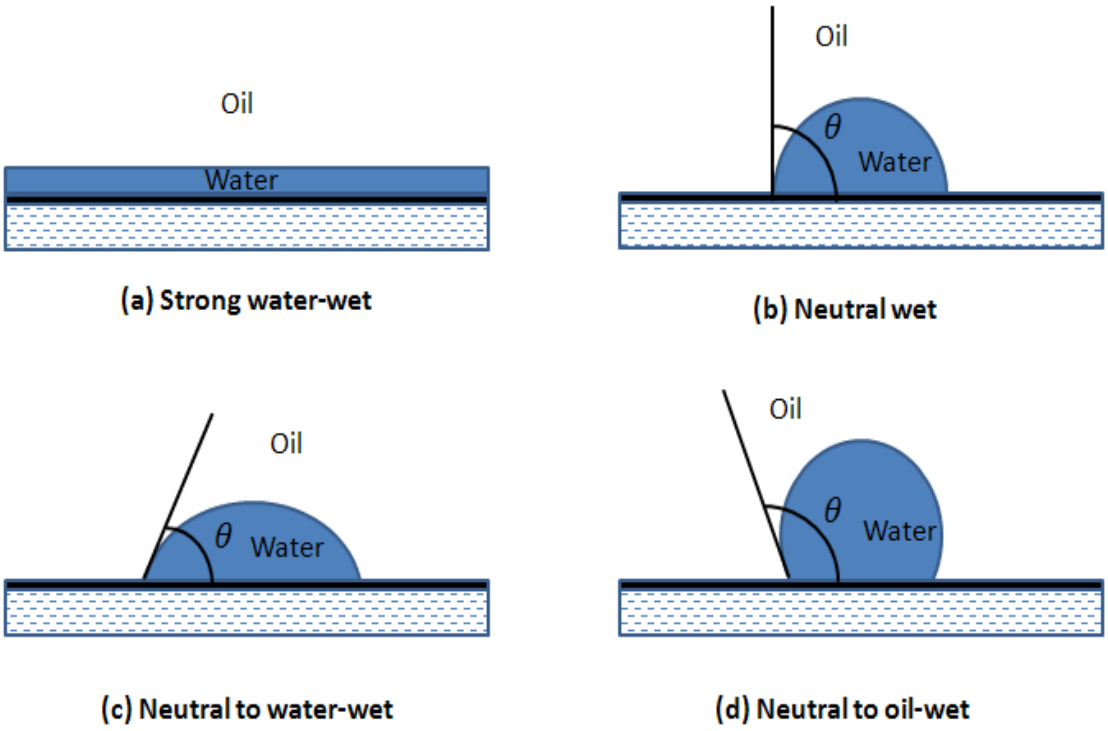

Figure A.1: Four different wettability cases: (a) Perfect water-wet formation. (b) Neutral wet formation. (c) Neutral to water-wet formation. (d) Neutral to oil-wet formation. Most water-wet rocks have equilibrium contact angles lower than 90°.

The Amott wettability index (I_w) is calculated as:

$$I_w = WI_w - WI_o \tag{A.1}$$

where WI_w and WI_o are the wettability indices of water and oil, respectively.

$$WI_w = \frac{Volume\ of\ oil\ displaced\ by\ water\ spontaneous\ imbibition}{Volume\ of\ oil\ displaced\ by\ water\ spontaneous\ imbibition\ +\ water\ forced\ displacement}, \tag{A.2}$$

and

$$WI_o = \frac{Volume\ of\ water\ displaced\ by\ oil\ spontaneous\ imbibition}{Volume\ of\ water\ displaced\ by\ oil\ spontaneous\ imbibition\ +\ water\ forced\ displacement} \quad \text{(A.3)}$$

Since the wettability indices of water and oil range from 0 to 1, the Amott wettability index will range from -1 (oil-wet rock) to +1 (water-wet rock), respectively.

A.2 United States Bureau of Mines (USBM) wettability test

USBM wettability test was developed by Donaldson et al. (1969). Reservoir core sample initially saturated with water is displaced with oil to irreducible water saturation. Then, the sample is centrifuged in water to residual oil saturation. Water in the sample is displaced again with oil to irreducible water saturation using the centrifuge. **Figure A.2** shows the capillary pressure curves along forced water and oil imbibition between irreducible water saturation and residual oil saturation. Since the area (A_1 and A_2) under the capillary pressure curves is proportional to the energy required to displace, this method can measure the thermodynamic work required for each forced imbibition. USBM wettability index, *W,* is defined as

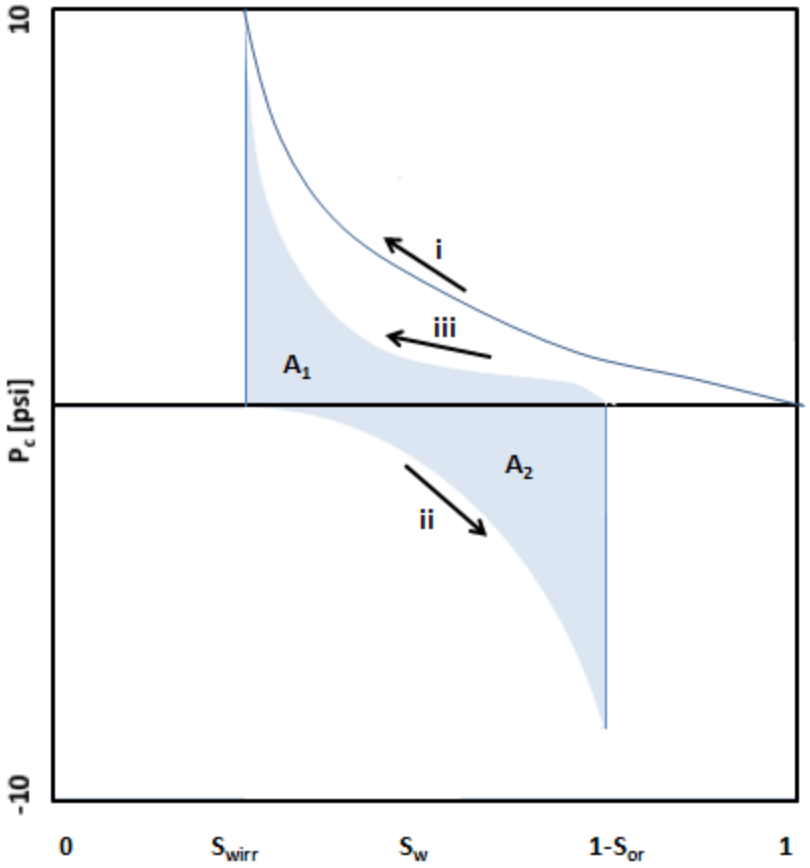

Figure A.2: USBM test to determine USBM wettability index. Areas under the capillary pressure curves, A_1 and A_2, represent energy required to displace water and oil, respectively.

$$W = \log_{10}\left(\frac{A_1}{A_2}\right) \tag{A.4}$$

USBM wettability index is determined by a logarithmic A_1/A_2 ratio, the value can be either positive (water-wet) or negative (oil-wet). The absolute value of USBM

wettability index is limited to 1, which is a strongly water-wet or a strongly oil-wet case. A medium of neutral wettability has a wettability index of 0 because A_1 and A_2 are equal.

Nomenclature

a	:	Archie's factor, [ ]
α	:	Regularization parameter, [ ]
Υ	:	Gyromagnetic ratio for hydrogen nuclei, [MHz/Tesla]
σ_{Dw}	:	Standard deviation of D_w distribution, log [ ]
σ_{Do}	:	Standard deviation of D_o distribution, log [ ]
σ_{Dg}	:	Standard deviation of D_g distribution, log [ ]
ρ_{sand}	:	Surface relaxivity for sand, [um/sec]
$\rho_{carbonate}$	:	Surface relaxivity for carbonate, [um/sec]
ρ_{clay}	:	Surface relaxivity for clay, [um/sec]
ρ_{Illite}	:	Density of Illite, [g/cc]
$\rho_{Montmorillonite}$	:	Density of Montmorillonite, [g/cc]
$\rho_{Chlorite}$	:	Density of Chlorite, [g/cc]
ρ_{Quartz}	:	Density of Quartz, [g/cc]
$\rho_{Dolomite}$	:	Density of Dolomite, [g/cc]
$\rho_{Calcite}$	:	Density of Calcite, [g/cc]
$\rho_{Siderite}$	:	Density of Siderite, [g/cc]
ρ_{Pyrite}	:	Density of Pyrite, [g/cc]
m	:	Archie's porosity exponent, [ ]
n	:	Archie's saturation exponent, [ ]
μ	:	Mean of Gaussian distribution, [ ]
σ_{shell}	:	Standard deviation of T_2 distribution of fluid in shell, [ ]
σ_{core}	:	Standard deviation of T_2 distribution of fluid in core, [ ]
AT90	:	Array induction resistivity [ohm.m]
B_0	:	Static magnetic field [Gauss]
B_1	:	Oscillating magnetic field [Gauss]
$C(a)$	:	Cost function, [ ]

D_{water} : Diffusion coefficient for water, log [μm^2/sec]

D_{oil} : Diffusion coefficient for oil, log [μm^2/sec]

D_{gas} : Diffusion coefficient for gas, log [μm^2/sec]

D : Diffusion coefficient, log [μm^2/sec]

D_w : Mean value of diffusion coefficient for gas, log [um^2/sec]

D_o : Mean value of diffusion coefficient for gas, log [um^2/sec]

$D_{\backslash g}$: Mean value of diffusion coefficient for gas, log [um^2/sec]

G : Magnetic field-strength gradient, [Gauss/cm]

HI_{water} : Hydrogen Index for water, [ ]

HI_{oil} : Hydrogen Index for oil, [ ]

HI_{gas} : Hydrogen Index for gas, [ ]

I_w : Amott wettability index, [ ]

k : Absolute permeability, [md]

k_r : Relative permeability, [md]

M : Amplitude of magnetization, [ ]

NE : Number of echoes, [ ]

P_c : Capillary pressure, [psi]

R_{sh} : Resistivity of shale, [Ohm-m]

R_w : Connate water resistivity, [Ohm-m]

S_{bw} : Bound water saturation, [V/V]

S_{fw} : Free water saturation, [V/V]

S_{wr} : Residual wetting phase saturation, [V/V]

S_{nwr} : Residual non-wetting phase saturation, [V/V]

S_w : Water saturation, [V/V]

S_{gas} : Oil saturation, [V/V]

S_{gas} : Gas saturation, [V/V]

TE : Inter-echo time, [ms]

T_1 : Longitudinal relaxation time, log [ms]

T_2 : Transverse relaxation time, log [ms]

$T_{1bulk,w}$: Bulk longitudinal relaxation time for water, [ms]

$T_{1bulk,o}$: Bulk longitudinal relaxation time for oil, [ms]

$T_{2bulk,w}$: Bulk transverse relaxation time for water, [ms]

$T_{2bulk,o}$: Bulk transverse relaxation time for oil, [ms]

TW : Polarization time, [ms]

T_1/T_2 : T_1 over T_2 ratio, [ ]

W_d : Data weighting matrix, [ ]

W_x : Model weighting matrix, [ ]

W : USBM wettability index, [ ]

WI_w : Wettability index of water, [ ]

WI_o : Wettability index of oil, [ ]

Acronyms

2D	:	Two Dimensional
3D	:	Three Dimensional
CPMG	:	Carr-Purcell-Meiboom-Gill
CSF	:	Common Stratigraphic Framework
DOI	:	Depth of Investigation
ECS	:	Elemental Capture Spectroscopy
GOR	:	Gas to Oil Ratio
GR	:	Natural Gamma-Ray Log
HI	:	Hydrogen Index
IFK	:	Fredholm integral equation of the first kind
NMR	:	Nuclear Magnetic Resonance
OBM	:	Oil Base Mud
PEF	:	Photo Electric Factor
PDF	:	Probability Density Function
RF	:	Radio frequency
SNR	:	Signal to Noise Ratio
SVD	:	Singular Value Decomposition
USBM	:	United States Bureau of Mines
UTAPWeLS	:	University of Texas at Austin's Petrophysical and Well Log Simulator

References

Amott, E, 1959, Observations relating to the wettability of porous rock, *Petroleum Transactions, AIME*, v. 216, pp. 216.

Aster, R., Borchers, B., and Thurber, C., 2005, Parameter estimation and inverse problems: *Elsevier Academic Press*, Burlington, Massachusetts.

Belgaised, A., Al-Farisi, O., Al-Ghusain, S., Al-Muntheri, H., Al-Marzouqi, M, and Petricola, M., 2004, Comparing the accuracy of fluid saturation derived from different logging measurements: past, present and future methodology, *SPE 11th Abu Dhabi International Petroleum Exhibition and Conference*, Abu Dhabi, U.A.E., October 10-13.

Bloembergen, N., Purcell, E. M., and Pound, R. V., 1947, Relaxation effects in nuclear magnetic resonance absorption, *Physical Review*, v. 73, no. 7, pp. 679-712.

Carr, H. Y. and Purcell, E. M., 1954, Effects of diffusion on free precession in nuclear magnetic resonance experiments, *Physical Review*, v. 94, no. 3, pp. 630-638.

Chen, J., Hirasaki, G.J., and Flaum, M., 2004, Effects of OBM invasion on irreducible water saturation: mechanisms and modifications of NMR interpretation, *SPE Annual Technical Conference and Exhibition*, Houston, Texas, USA, September 26-29.

Clavier, C., Coates, G. R., and Dumanoir, J., 1984, Theoretical and experimental bases for the dual-water model for interpretation of shaly sands, *SPE Journal*, v. 24, no. 2, pp. 153-168.

Coates, G. R., Xiao, L., and Prammer, M. G., 1999, NMR logging principles and applications, Halliburton Energy Services.

Donaldson, E. C., Thomas, R. D., and Lorenz, P. B., 1969, Wettability determination and its effect on recovery efficiency, *SPE Journal*, v. 9, no. 1, pp. 13-20.

Dunn, K.-J., Bergman, D. J., and Latorraca, G. A., 2002, Nuclear magnetic resonance petrophysical and logging applications, *Handbook of Geophysical Exploration*, v. 32.

Freedman, R., Heaton, N., Flaum, M., Hirasaki, G.J., Flaum, C., and Hürlimann, M., 2003, Wettability, saturation, and viscosity from NMR measurements, *SPE Journal*, v. 8, no. 4, pp. 317-327.

George, K., 2003, A case study integrating the physics of mud-filtrate invasion with the physics of resistivity logging, Master's Thesis, The University of Texas at Austin.

Hansen, P. C., 2007, Regularization Tools: A Matlab package for analysis and solution of discrete ill-posed problems: *Numerical Algorithms*, v. 46, no. 2, pp. 189-194.

Heaton, N.J., Minh, C, Kovats, J., and Guru, U., 2004, Saturation and viscosity from multidimensional nuclear magnetic resonance logging, *SPE Annual Technical Conference and Exhibition*, Houston, Texas, USA, September 26-29.

Jerath, K., 2011, Reconciliation of two-dimensional NMR measurements with the process of mud-filtrate invasion mud-filtrate invasion: synthetic and field examples, Master's Thesis, The University of Texas at Austin.

Kausik, R., Minh, C. C., Zielinski, L., Vissapragada, B., Akkurt, R., Song, Y., Liu, C., Jones, S., and Blair, E., 2011, Characterization of gas dynamics in kerogen nanopores by NMR, *SPE Annual Technical Conference and Exhibition*, Denver, Colorado, USA, October 30-November 2.

Kenyon, W. E., Howard, J. J., Sezginer, A., Straley, C., and Matteson, A., 1989, Pore-size distribution and NMR in microporous cherty sandstones, *SPWLA 30th Annual Logging Symposium*, New Orleans, Louisiana, USA, June 11-14.

Kenyon, W. E., 1997, Petrophysical principles of applications of NMR logging, *The Log Analyst*, v. 38, no. 2, pp. 21-43.

Klein, J. D., and Martin, P. R., 1997, Log water saturation model validation using NMR log and core data, *SPWLA 38th Annual Logging Symposium*, Jakarta, Indonesia, June 15-18.

Lo, S-W, Hirasaki, G. J., House, W. V., and Kobayashi, R., 2002, Mixing rules and correlations of NMR relaxation time with viscosity, diffusivity, and gas/oil ratio of methane/hydrocarbon mixtures, *SPE Annual Technical Conference and Exhibition*, Dallas, Texas, USA, October 1-4.

Looyestijn, W. J., and Hofman, J. P., 2006, Wettability index determination by nuclear magnetic resonance, *SPE Journal*, v. 9, no. 2, pp. 146-153.

Meiboom, S., and Gill, D., 1958, Modified spin echo method for measuring nuclear relaxation times, *Review of Scientific Instruments*, v.29, pp. 688-691.

Minh, C. C., Heaton, N., Ramamoorthy, R., Decoster, E., White, J., Junk, E., Eyvazzadeh, R., Al-Yousef, O., Fiorini, R., and Mclendon, D., 2003, Planning and interpreting NMR fluid-characterization logs, *SPE Annual Technical Conference and Exhibition*, Denver, Colorado, USA, October 5-8.

Simandoux, P., 1963, Dielectric measurements in porous media and application to shaly formation: *Revue de L'Institut Français du Pétrole*, v. 18, Supplementary Issue, p.193-215.

Steene, M. V., Ardila, M., Nelson, R., Fekry, A., and Farghaly, A., 2012, Fluid identification in light hydrocarbons using NMR and downhole fluid analyzers, *SPE North Africa Technical Conference and Exhibition*, Cairo, Egypt, February 14-17.

Straley, C., Rossini, D., Vinegar, H., and Tutunjian, P., 1994, Core analysis by low field NMR, *International symposium of the Society of Core Analysts*, Stavanger, Norway, September 12-14.

Sun, B., and Dunn, K-J., 2005, A global inversion method for multi-dimensional NMR logging, *Journal of Magnetic Resonance*, v. 172, issue 1, pp. 152-160.

Tikhonov, A. N., and Arsenin, V. Y., 1977, Solution of ill-posed problems. Baltimore, MD: Winston and Sons.

Timur, A., 1969, Pulsed nuclear magnetic resonance studies of porosity, movable fluid, and permeability of sandstones, *Journal of Petroleum Technology*, v. 21, no. 6, pp. 775-786.

Toumelin, E., and Torres-Verdín, C., 2002, Quantification of multi-phase fluid saturations in complex pore geometries from simulations of Nuclear Magnetic Resonance measurements, *SPE Annual Technical Conference and Exhibition*, San Antonio, Texas, USA, September 29-October 2.

Toumelin, E., Torres-Verdín, C., Sun, B., and Dunn, K-J., 2004, A numerical assessment of modern borehole NMR interpretation techniques, *SPE Annual Technical Conference and Exhibition*, Houston, Texas, USA, September 26-29.

Toumelin, E., and Sun, B., 2009, Optimization of wireline NMR pulse sequences, *SPWLA 50th Annual Logging Symposium*, The Woodlands, Texas, USA, June 21-24.

Voss, B., Torres-Verdín, C., Gandhi, A., Alabi, G., and Lemkecher, M., 2009, Common Stratigraphic Framework to simulate well logs and to cross-validate static and dynamic petrophysical interpretations, *SPWLA 50th Annual Logging Symposium*, The Woodlands, Texas, USA, June 21-24.

Washburn, K. E., and Birdwell, J. E., 2013, Updated methodology for nuclear magnetic resonance characterization of shales, *Journal of Magnetic Resonance*, v. 233, issue 1, pp. 17-28.

Zhang, G. Q., Huang, C-C., and Hirasaki, G. J., 2000, Interpretation of wettability in sandstones with NMR analysis, *International Symposium of the Society of Core Analysts*, Golden, Colorado, USA, August 1-4.